ELSEVIER

Efficiently multifunctional catalysts of 3D ordered meso-macroporous Ce$_{0.3}$Zr$_{0.7}$O$_2$-supported PdAu@CeO$_2$ core-shell nanoparticles for soot oxidation: Synergetic effect of Pd-Au-CeO$_2$ ternary components

Jing Xiong, Xuelei Mei, Jian Liu, Yuechang Wei*, Zhen Zhao, Zean Xie, Jianmei Li

State Key Laboratory of Heavy Oil Processing, College of Science, China University of Petroleum, Beijing, China

ARTICLE INFO

ABSTRACT

Efficiently multifunctional catalyst of PdAu@CeO$_2$ core-shell nanoparticles supported on 3D ordered meso-macroporous Ce$_{0.3}$Zr$_{0.7}$O$_2$ (PdAu@CeO$_2$/3DOMM-CZ) was elaborately synthesized by gas bubbling-assisted membrane reduction-precipitation (GBMR/P) method. The uniform 3DOMM structure with the larger surface area improves the contact efficiency between reactants (O$_2$, NO and soot) and catalysts, and increases the density of supported active sites. The nanostructure of AuPd (core) and CeO$_2$ layer (shell) with optimal interface area of metal-oxides increases the surface density of active oxygen species (oxygen vacancy) for enhancing adsorption and activation of O$_2$ and NO reactants. PdAu@CeO$_2$/3DOMM-CZ catalyst, which takes both advantages of the good contact efficiency between reactants and catalysts by 3DOMM structure and the high density of active sites for activated reactants (O$_2$ and NO) by PdAu@CeO$_2$ core-shell NPs, exhibited super catalytic performance for soot oxidation under conditions of the simulated real exhaust including NO, soot, N$_2$, O$_2$ and H$_2$O. For instance, its TOF value is 2.51 h^{-1} at 290 °C, which is more than 5-fold increase for 3DOMM-CZ oxide (0.46 h^{-1}), and the values of T$_{10}$, T$_{50}$, T$_{90}$ are 276, 363, 404 °C, respectively. PdAu@CeO$_2$/3DOMM-CZ catalyst exhibits the high stability and the good tolerance property for SO$_2$ during catalytic soot oxidation. The catalytic mechanism for soot oxidation was investigated by in-situ Raman spectra, and the synergetic effect of Pd-Au-CeO$_2$ ternary active components can promote the rate determining step of NO oxidation to NO$_2$. Insight into the fabrication strategy and the catalytic mechanism for soot oxidation are expected to further obtain the high-efficient catalyst in the practical applications.

1. Introduction

The problem of air pollution has caused significant risk for ecological environment and human health. In particular, soot particles emitted from mobile diesel engines is the main source for atmospheric contamination and secondary pollution [1]. The technology of continuously regenerating particle trap (CRT) with combination of filter and catalyst is one of the most efficient after-treatment techniques for diesel soot reduction [2]. The finding high-performance catalyst for soot oxidation at the relatively low temperature is a challenge. A series of high efficiency catalysts for soot oxidation have been studied, such as supported noble metal nanoparticles [3,4], transition metal oxides [5–8], Ce-based oxides [9–12], perovskite type oxides, [13,14] alkaline metal oxides [15,16], and so on. Among them, Ce-based oxide is one of the critical components in vehicle exhaust purification catalysts due to the excellent redox properties and oxygen storage/release capacity, and

Ce atoms in CeO$_2$ crystal lattice can be replaced by Zr or Nd cations to form Ce$_x$M$_{1-x}$O$_2$ solid solutions, which will improve the thermal stability. [17,18]

The catalytic reaction of soot oxidation takes place at a three-phase boundary among a solid catalyst, a solid reactant (soot), and gaseous reactants (O$_2$, NO). The catalytic performance for soot oxidation is mainly affected by two aspects: the contact efficiency between active sites and reactants (soot, O$_2$ and NO), and the intrinsic activity of active sites for activation and oxidation of reactants [19–21]. The reaction of catalytic soot oxidation is a complex heterogeneous catalysis, and the nanostructure of catalyst plays a determining role in the process of soot combustion. The contact efficiency of catalyst-soot and catalyst-gaseous reactants (O$_2$ and NO) can be improved by the macroporous and mesoporous structures, respectively. For the general catalysts, they possess imporous or the smaller pore sizes (< 10 nm) in comparison with the diameters (20–1000 nm) of soot particles. Thus, their catalytic

oxidation performance would be restricted by the poor contact efficiency of catalyst-soot particles and the lacking surface density of active sites [22,23]. In order to increase contact efficiency between catalyst and soot, the fabricating catalysts with macroporous structure is a practicable solution way [24–27]. In our previous works [28,29], it was found that three-dimensionally ordered macroporous (3DOM) catalysts with large pore size (> 200 nm) can not only assist soot particles to enter their inner pores, but also permit soot particles through the porous structure easily and less diffusion resistance to access the surface active centers. Therefore, 3DOM catalysts with excellent contact efficiency between catalyst and soot exhibited better catalytic performance for soot oxidation compared with the disordered macroporous or powder catalysts.

For improving contact efficiency between catalyst and gaseous reactants (NO and O_2), the fabricating ordered mesoporous nanostructure is benefit for enhancing adsorption and activation capacities for gaseous reactants (NO and O_2) [30]. The ordered mesoporous structure can improve specific surface area, which will offer more active sites for activated O_2 and catalytic NO oxidation to NO_2 with the high oxidation ability as the effective intermediate species [31]. The formation of NO_2 would transform the reaction modes from solid (catalyst)-solid (soot)-gas (O_2) into solid (catalyst)-gas (NO_2)-solid (soot). Thus, the contact efficiency of soot-catalyst can be improved indirectly. Combining ordered macroporous and mesoporous nanostructure, the fabrication of three-dimensionally ordered meso-macroporous (3DOMM) catalysts can improve both contact efficiency of catalyst-soot and catalyst-gas (NO and O_2) simultaneously. Therefore, it is expected to enhance the catalytic activity for soot oxidation via the fabricating of 3DOMM nanostructure.

For enhancing the intrinsic redox capacity for soot oxidation, the nanostructure and composition of active components should be taken into consideration [32]. Utilizing noble metal (Pt, Au, Pd) as active component can promote adsorption-activation capacity for gaseous oxygen and increase the surface density of active oxygen species [33]. Combining two noble metal components to form bimetallic active sites is an efficient way to tune the atomic scale characteristics and improve the utilization of each effective component [34–37]. It is worth mentioned that Hutchings and co-authors have achieved a series of groundbreaking research results of Au-based alloy catalysts in the field of heterogeneous catalysis, in particular, the PdAu catalysts [38,39]. And the catalytic performance of complex nanostructures for deep catalytic oxidation often depend on the strong metal-support interaction (SMSI) at the interface of supported noble metal NPs and oxides [40]. Core-shell nanostructure can optimize the interface areas between metal active sites and oxide support, and increase the surface density of active sites induced by the SMSI effect [41–43]. The shape-controlled fabrication of 3DOMM oxides supported noble metals@oxides core-shell nanoparticle catalysts at the nanoscale is a practical route for improving catalytic activity and stability for soot oxidation. However, the assembly of core-shell nanoparticles deposited on the inner surface of 3DOMM composite oxide is still a great challenge.

Herein, the multifunctional catalysts of PdAu@CeO$_2$ core-shell NPs supported on 3DOMM Ce$_{0.3}$Zr$_{0.7}$O$_2$ solid solution (PdAu@CeO$_2$/3DOMM-CZ) were successfully synthesized via the methods of evaporation-induced self-assembly colloidal crystal templates (EISA-CCT) and gas bubbling-assisted membrane reduction-precipitation (GBMR/P). The nanostructure of 3D ordered meso-macropores is beneficial for improving the contact efficiency of catalysts and reactants (soot, O_2 and NO), and the core-shell nanostructure of supported PdAu@CeO$_2$ active sites with the optimal SMSI effect can promote adsorption and activation capacities for gaseous reactants. PdAu@CeO$_2$/3DOMM-CZ catalyst, which combines of both the good contact efficiency between catalysts and reactants and the synergetic effect of Pd-Au-CeO$_2$ ternary active components, showed excellent catalytic activity and prominent nanostructure-dependent activity relationship for soot oxidation under the simulated real exhaust condition including NO, soot, N_2, O_2 and H_2O.
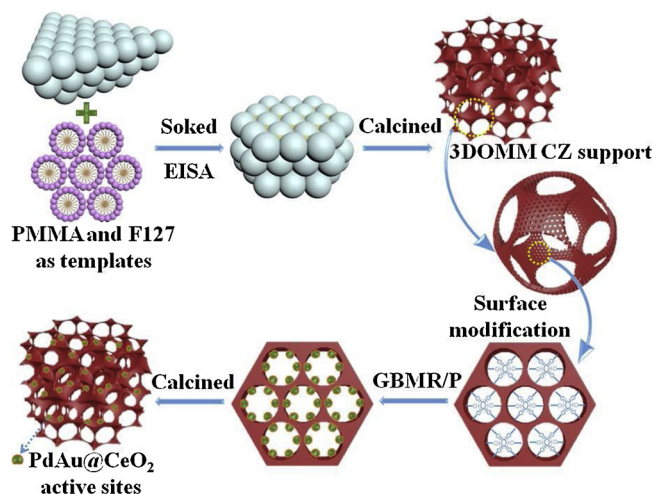

Fig. 1. Fabrication schematic of PdAu@CeO$_2$/3DOMM-CZ catalyst by combined methods of EISA-CCT and GBMR/P.

2. Experimental

2.1. Synthesis of catalysts

2.1.1. Synthesis of 3DOMM Ce$_{0.3}$Zr$_{0.7}$O$_2$ solid solution

Preparation of monodispersed polymethyl methacrylate (PMMA) microspheres and assembly of templates are similar to that described previously [25]. The typical preparation procedures of PdAu@CeO$_2$/3DOMM-CZ catalysts are shown in Fig. 1. 3DOMM CZ was synthesized by EISA-CCT method. [44] F127 as the mesoporous template was added into the Ce/Zr precursor solution, and then the mixture was soaked into the gaps of CCT. The CCT and F127 templates were removed by calcination at the rising temperature rate of 2 °C min^{-1} from 50 to 500 °C in the air ambient and continued at 500 °C for 4 h. Finally, 3DOMM Ce$_{0.3}$Zr$_{0.7}$O$_2$ composite oxide was obtained and was abbreviated as 3DOMM CZ. The detailed preparation processes of PMMA and 3DOMM CZ support are shown in the *Experimental Section of Supporting information*.

2.1.2. Synthesis of 3DOMM CZ-supported Pd, Au, PdAu and PdAu@CeO$_2$ NPs catalysts

3DOMM CZ supported Pd, Au and PdAu binary NP catalysts were synthesized by the GBMR method, while 3DOMM CZ-supported PdAu@CeO$_2$ core-shell NP catalyst was synthesized by the one-pot process of gas bubbling-assisted membrane reduction-precipitation (GBMR/P) method [45]. The typical synthesis processes were shown as follows: 3DOMM CZ support (0.5 g) was dispersed in 200 ml deionized water under vigorous stirring. The solution of Pd(NO$_3$)$_2$ and HAuCl$_4$ was mixed uniformly and added into the CZ slurry. The loadings of Pd and Au in PdAu/3DOMM-CZ and PdAu@CeO$_2$/3DOMM-CZ catalysts are 2 wt% in theory, respectively. The poly (N-vinyl-2-pyrrolidone) (PVP) solution (20 ml, 1.275 mol L^{-1}) as a stabilizer was added into the mixed solution. All reactants formed a cycling flow between glass tube reactor and beaker driven by a peristaltic pump at the rate of 300 ml min^{-1}. Meanwhile, NaBH$_4$ solution (40 ml, 0.5 g L^{-1}) as the reductant was injected into the membrane reactor at a slow rate of 0.6 ml min^{-1} by a constant flow pump. Through the abundant holes (d = 40 nm) on the walls of the ceramic tubes, the NaBH$_4$ solution was infiltrated into the glass tube reactor equally, where two solutions met and the reduction of metal ions occurred immediately. The bubbles of hydrogen outside the tube wall facilitate the reduction process and make the reaction homogenously. The color of the slurry changes from light yellow to dark grey, and PdAu/3DOMM-CZ catalyst can be obtained just by filtration and calcination. After the NaBH$_4$ solution was

consumed completely, the $Ce(NO_3)_3$ solution (15 ml, 5 g L^{-1}) was introduced into the reaction system, while ammonia solution (1 wt%) as precipitator was injected into the membrane reactor at a slow rate of 0.8 ml min^{-1}. When the ammonia solution consumed completely and aged for one hour, the products were filtered and washed with distilled water. Then the final product was calcined in a tube furnace at 500 °C for 3 h and the desired PdAu@CeO$_2$/3DOMM-CZ catalyst was obtained. Detailed information about the reagent specifications are shown in Table S1. For comparison, Pd/3DOMM-CZ and Au/3DOMM-CZ catalysts (the initial weight percents of Pd or Au ions to CZ support were always 4 wt%) were synthesized via the same GBMR procedures.

2.2. Catalysts characterization

The surface morphology and structure of the catalysts were carried out on a SEM with accelerating voltage 5 kV (ZEISS Gemini SEM 300). The TEM images of 3DOMM oxide and supported NPs were obtained on the JEOL JEM LaB$_6$ 2100 electron microscope. High angle annular dark field (HAADF) images in scanning transmission electron microscope (STEM) mode and energy-dispersive X-ray spectroscopy (EDX) analyses were carried out on an FEI Tecnai G2 F20 transmission electron microscope operating at 200 kV. Nitrogen adsorption-desorption experiments were operated on a Micromeritics TriStar-II 3020 instrument. The crystal phase and ordered mesoporous nanostructure were investigated by powder X-ray diffraction (XRD) spectrometer (Bruker D8 Advance) with Cu Kα radiation (λ = 1.54184 Å). The actual amounts of Au and Pd in the catalysts were determined by inductive coupled plasma optical emission spectrometry (ICP-OES, Perkin Elmer, OPTIMA 7300 V). Raman spectra were carried out on an inVia Reflex-Renishaw spectrometer in the anti-Stokes range of 100-1500 cm^{-1}. The catalysts were excited using a He-Ge laser (excitation wavelength 532 nm). In-situ Raman spectra were conducted on the same high-resolution Raman spectrometer system. For in-situ Raman measurements, the catalysts were deposited on an in-situ cell with a quartz window. The sample was pretreated in a He gas flow (50 ml min^{-1}) at room temperature for 30 min. Then the reaction atmosphere switched to O$_2$ (5%) and NO (0.2%) balanced with He (50 ml min^{-1}) and the temperature increased to 450 °C at a heating rate of 10 °C min^{-1}. The spectra were recorded the variation of all peaks at desired temperature. X-ray photoelectron spectra (XPS) were performed on a XPSPHI-1600 ESCA spectrometer using the X-ray source of Al Kα anode (hν = 1253.6 eV). The hydrogen (H$_2$) temperature-programmed reduction measurements (H$_2$-TPR) were carried out on a fixed-bed device. The catalyst (50 mg) was firstly treated by N$_2$ ambient at 300 °C for 30 min and cooled subsequently to room temperature. The gas flow of 10% H$_2$/N$_2$ (50 ml min^{-1}) then passed the catalyst in the range of 30–900 °C at rising rate of 10 °C min^{-1}. The TCD detector was used to monitor the signal of H$_2$ consumption. The NO temperature-programmed oxidation (NO-TPO) were carried out on a fixed-bed tubular quartz reactor (φ = 8 mm). The reactant gas flow is 50 ml min^{-1} containing 5% O$_2$ and 2000 ppm NO balanced with N$_2$. The catalyst was pretreated in N$_2$ flow at 200 °C for 30 min. Then gaseous reactants passed the fixed-bed reactor at a rising temperature rate of 2 °C min^{-1} from 100 to 500 °C. The outlet gases were monitored by FT-IR spectra at the desired temperature.

2.3. Catalytic performance evaluation

The catalytic performances of the catalysts for soot oxidation were evaluated by temperature-programmed oxidation (TPO) reaction, and each soot-TPO test ranges from 100 to 550 °C at the rising rate of 2 °C min^{-1}. The carbon powder of Printex-U (diameter~25 nm) was used as the model soot particles. The catalyst (100 mg) and soot particle (10 mg) were mixed to the loose contact mode by using a spoon in order to simulate the actual conditions of catalytic soot purification. The flow rate of gaseous reactants is 50 ml min^{-1} containing of O$_2$ (5 vol %), NO (0.2 vol %) and H$_2$O (5 vol %) or SO$_2$ (0.02 vol %) balanced with Ar.

The outlet gaseous products were analyzed by an online GC with an FID detector (9890, Shanghai). The catalytic activity for soot oxidation is estimated by the values of T_{10}, T_{50}, and T_{90}, which were defined as the temperatures of soot conversion of 10%, 50%, and 90%, respectively. The selectivity of CO$_2$ product (S_{CO2}) in the products of soot oxidation was defined as the equation: $S_{CO2} = C_{CO2}/(C_{CO} + C_{CO2})$. S_{CO2}^m was denoted as the S_{CO2} at which the C_{CO2} was the maximum.

The turnover frequency (TOF) of the catalysts representing the intrinsic activities was defined as the ratio of isothermal reaction rate to the surface density of active sites. The isothermal reaction rates for soot oxidation were obtained at a stable and small conversion of soot particles with an approximate kinetic regime. The isothermal reaction of soot oxidation was carried out at 290 °C because the soot conversion was low (< 10%) and the reaction rate was nearly constant during testing process. The composition of reaction gas was same as the soot-TPO reaction process containing of O$_2$ (5 vol %), NO (0.2 vol %) and H$_2$O (5 vol %) balanced with Ar. Reaction rate (R) for soot oxidation was obtained by the analyses of gaseous products. The density of catalytic active sites was calculated by isothermal anaerobic titration method at 290 °C. After the concentration of CO$_2$ product was stable, O$_2$ was instantaneously removed from the gaseous reactant. The data of CO$_2$ concentration with transient decay from the steady state was collected by an online GC with the FID detector.

3. Results

3.1. Fabrication mechanism of PdAu@CeO$_2$/3DOMM-CZ catalyst

The syntheses of 3DOMM CZ-supported PdAu bimetallic alloy NPs and PdAu@CeO$_2$ core-shell NPs catalysts are primary goals to improve catalytic performance for soot oxidation and still great challenges. Fig. 1 shows the fabrication schematic of PdAu@CeO$_2$/3DOMM-CZ catalyst by EISA−CCT and GBMR/P methods. In the fabrication processes of 3D ordered mesoporous-macroporous (hierarchical porous) nanostructure, polymeric surfactant F127 as the mesopores template plays a critical role to obtain 2D hexagonal (p6mm) ordered mesoporous structure. Meanwhile, PMMA microspheres as the macroporous template dominate the formation of 3D ordered macroporous framework. For the combined method of EISA−CCT, F127 was added into the Ce-Zr precursors to form a mixture and then filled into the interstices of CCT to fabricate 3D ordered macroporous framework. In the following, the solid-liquid mixtures were dried mildly under the saturated vapor pressure condition at 50 °C. With increasing of the F127 concentration, the saturated micelles would arrange in the two-dimensional hexagonal order spontaneously. Meanwhile, Ce and Zr ions were attracted to the ordered arrangements around the micelles to form the mesoporous nanostructure. The EISA procedure is critical to form the ordered mesoporous nanostructure on the walls of macropores. Finally, the semi-finished products were calcined to remove templates (PMMA and F127), and 3DOMM CZ oxide support with hierarchical porous nanostructure was obtained.

In the fabrication process of core-shell structured PdAu@CeO$_2$ NPs, the homogeneous dispersion of reductant and precipitant is critical to control the nucleation and growth of supported core-shell nanoparticles. The key part of GBMR/P device is the membrane reactor, which consists of four ceramic tubes with plentiful holes (d = 40 nm) on the walls [46]. The two of membrane tubes were used to introduce reductant or precipitant (NaBH$_4$ or ammonium solution) into reaction system, and the other two tubes were used to blow H$_2$ gas membrane, which is benefit for mixing the reactants uniformly. At the beginning, Pd and Au ions were adsorbed by surface [OH]$^−$ groups on the surface of CZ oxide when the pH value of the solution is higher than the isoelectric point (IEP) of CZ support. When the NaBH$_4$ solution was infiltrated into the tubular reactor by the pores of ceramic membrane tubes, the reduction of adsorbed metal ions occurred immediately to form tiny nucleus and further growth of crystal nucleus on the surface
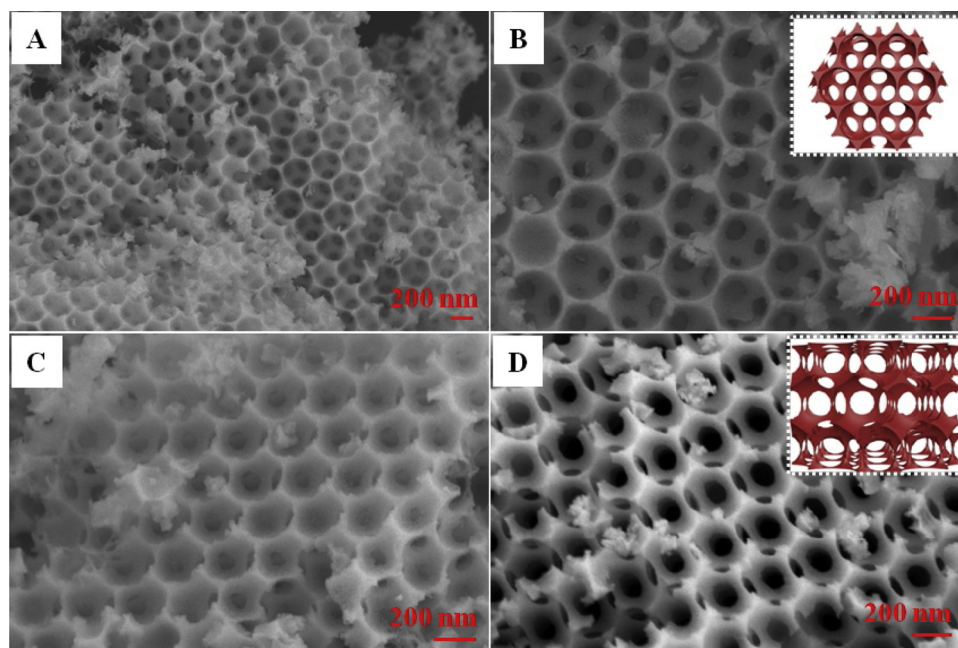
Fig. 2. SEM images of 3DOMM CZ support (A–B), PdAu/3DOMM-CZ (C) and PdAu@CeO$_2$/3DOMM-CZ (D) catalysts.

of 3DOMM CZ support. Thus, the uniform distribution of PdAu binary alloy NPs (cores) with PVP stabilizer deposited on 3DOMM CZ can be achieved facilely. Next, the precipitant of NH$_3$·H$_2$O solution was infiltrated into the tubular reactor, and Ce ions precipitated immediately to give a hydroxide shell covering on the surface of PdAu binary NPs. By controlling the flow rate of precipitation agent and cycle rate of reaction mixture, the dispersion and nanostructure of core-shell PdAu@CeO$_2$ NPs can be effectively controlled by the GBMR/P method. The color of reaction mixture changed from dark grey to light grey, indicating that the hydroxide were linked with metal core and partly covered the metal cores due to the complexation of AuPd-Ce(OH)$_3$ with PVP as chelating agent. Finally, the as-prepared product was calcined to remove PVP, and the desired PdAu@CeO$_2$/3DOMM-CZ catalyst was obtained.

3.2. SEM images

The structure and morphology of 3DOMM CZ, PdAu/3DOMM-CZ and PdAu@CeO$_2$/3DOMM-CZ catalysts were investigated by means of SEM technique, and the results are shown in Fig. 2. From the images of Fig. 2A and B, CZ support possesses the 3D ordered macroporous structure containing the framework surrounding uniform close-packed periodic voids, which is derived from the long-range replication of 3D close-packed PMMA template. The average diameter of macropores (~240 nm) correspond to shrinkage of 20–30 % in comparison with the sizes of PMMA microspheres (290 nm) in Fig. S1, which is caused by the melting of PMMA templates and the sintering of the produced metal oxides during calcination process for removing CCT and F127 templates. In addition, the thickness of macroporous wall is ca. 30 nm. The next layer is highly visible and the voids are interconnected through the open windows, ca. 80 nm in diameter. As shown in Fig. 2C and D, after supported PdAu bimetallic NPs and PdAu@CeO$_2$ core-shell NPs, the 3D ordered macroporous structure has not changed or destroyed, indicating that the GBMR/P process rarely damaged the nanostructure of the catalysts. Moreover, the model insets in Fig. 2B and D show vividly that there are penetrating channels in 3DOMM structure from any direction, which are extreme conducive to the transmission and diffusion of reactants (soot, O$_2$ and NO).

3.3. TEM and HAADF-STEM images

The microstructures of 3DOMM CZ, PdAu/3DOMM-CZ and PdAu@CeO$_2$/3DOMM-CZ catalysts were further investigated by TEM and HAADF-STEM images, and the results are shown in Fig. 3. As shown in Fig. 3A and B, 3DOMM CZ support possesses clear three-dimensionally ordered macroporous framework with overlapped open windows. The diameter sizes of macropores are about 240 ± 10 nm, and the diameters of open windows interconnected voids are about 80 ± 5 nm, which is matched with the results observed by SEM images. The 3D ordered macropores permit large size reactants into their inner porous structure and decrease the diffusion resistance. It is benefit for enhancing the contact efficiency between catalysts and reactants. As shown in Fig. 3B, there are plenty of mesopores arrayed in two-dimensional ordered style over the inner wall of macropores, indicating that 3D ordered hierarchical nanostructure of meso-macropores is reliably formed. And the average diameter sizes of mesopores are about 4~5 nm. It is well known that the ordered mesoporous nanostructure on the frameworks of 3DOMM CZ can improve the specific surface area remarkably, which is benefit for enhancing the surface density of supported core-shell active sites to promote the absorption and activation properties for gaseous reactants (O$_2$ and NO). After supported PdAu bimetallic NPs (Fig. 3C) or PdAu@CeO$_2$ core-shell NPs (Fig. 3D), 3D ordered hierarchical nanostructure of meso-macropores has not changed. Moreover, highly dispersed NPs with the uniformed size are observed on the inner surface of 3DOMM CZ support. For PdAu/3DOMM-CZ catalyst, supported bimetallic PdAu NPs shows the narrow size distribution in the range of 1~5 nm, and the average size is about 3.2 nm (Fig. S2F and). For PdAu@CeO$_2$/3DOMM-CZ catalyst, the average size of PdAu@CeO$_2$ core-shell NPs is about 4.0 nm (Fig. S3), and the thickness of shell (inset in Fig. 3D) is about 0.5~1 nm.

Fig. 3E shows the HAADF-STEM images of PdAu@CeO$_2$/3DOMM-CZ catalyst. It can further observe the microstructure of ordered mesopores and supported PdAu@CeO$_2$ core-shell NPs dispersed on the wall of macropores. In order to investigate the composition of supported core-shell NPs, the HAADF-STEM EDX mapping analyses of Ce, Pd and Au elements over the typical PdAu@CeO$_2$/3DOMM-CZ catalyst are performed and the results are shown in Fig. 3F. The image exhibits one individual PdAu@CeO$_2$ NP with the size about 4 nm. The composition distributions of each elements in the core-shell NP were revealed
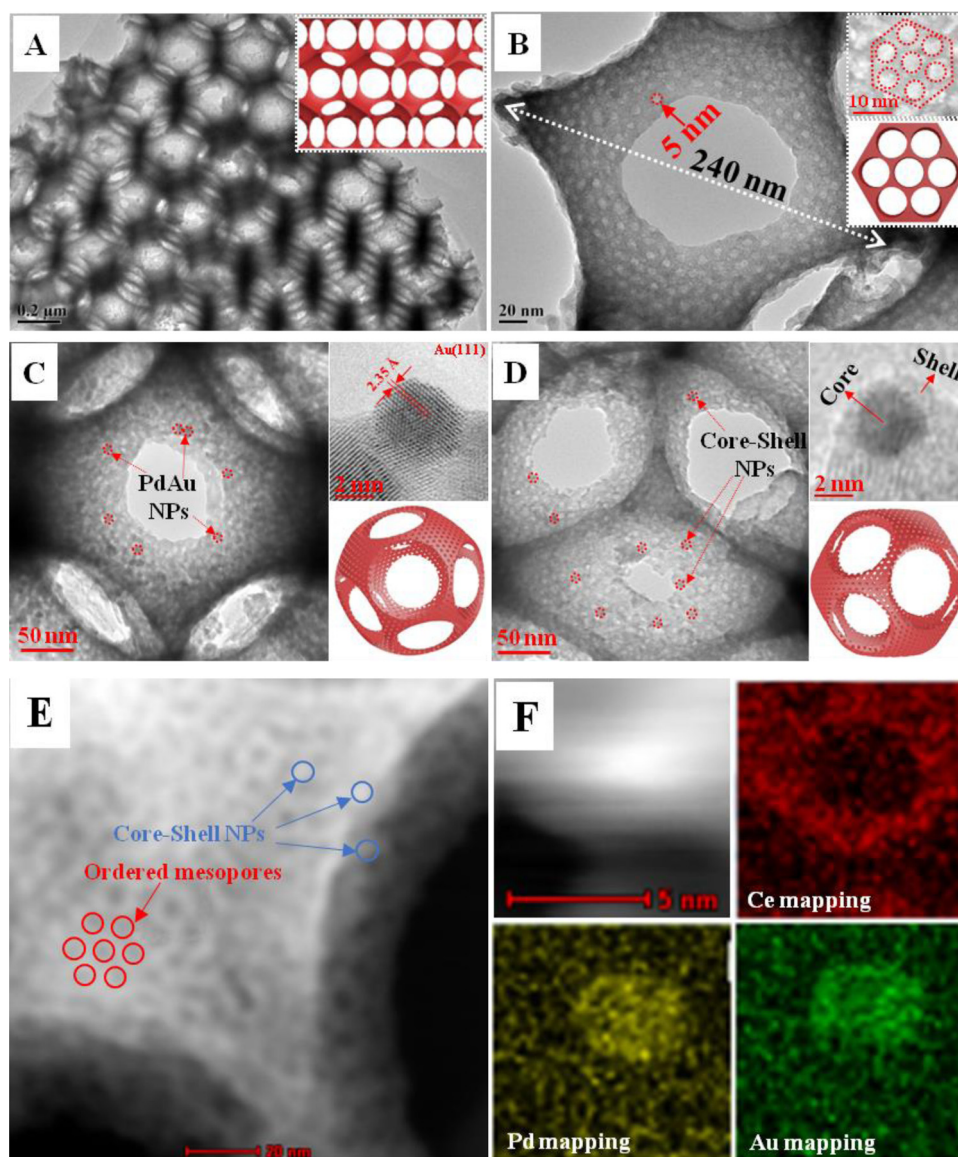
Fig. 3. TEM, HRTEM and HAADF-STEM images of 3DOMM CZ (A–B), PdAu/3DOMM-CZ (C) and PdAu@CeO$_2$/3DOMM-CZ (D–F) catalysts. The (F) image shows HR-STEM image of one PdAu@CeO$_2$ core-shell NP and its HAADF-STEM-EDX element-mapping analyses of Ce (red), Pd (yellow) and Au (green) (For interpretation of the references to colour in this figure legend, the reader is referred to the web version of this article).

by the EDX elemental mapping analysis. The images of Pd (yellow) and Au (green) elements are overlapped at the same area, indicating that the particle is one Pd-Au bimetallic alloy NP. Meanwhile, the Ce (red) element is mainly distributed around the PdAu NP (core) and forms the shell layers to protect the bimetallic NP. The core-shell nanostructured NPs could provide plenty of active sites with low-coordinatively unsaturated ceric cations and enhance the sintering resistance of Pd-Au bimetallic NPs because of the maximal contact region of CeO$_2$ (shell)-PdAu (core)-CZ (support) nanojunction system at the atomic level.

Table 1
BET surface areas, pore sizes, supported NP sizes of ordered mesoporous CZ, 3DOMM CZ, Pd/3DOMM-CZ, Au/3DOMM-CZ, PdAu/3DOMM-CZ and PdAu@CeO$_2$/3DOMM-CZ catalysts.

Catalysts	Mesoporous size (nm)[a]	S_{BET} (m^2 g^{-1})	Size of supported NPs (nm)[b]	Pd content (mmol g$_{cat}$$^{-1}$)[c]	Au content (mmol g$_{cat}$$^{-1}$)[c]
Mesoporous CZ	4.8	112	–	–	–
3DOMM CZ	4.9	75	–	–	–
Pd/3DOMM-CZ	4.7	70	3.1	0.49	–
Au/3DOMM-CZ	4.8	60	3.2	–	0.20
PdAu/3DOMM-CZ	4.8	57	3.2	0.26	0.11
PdAu@CeO$_2$/3DOMM-CZ	4.7	55	4.0	0.25	0.10

[a] Pore sizes of ordered mesoporous structure obtained by BET method.
[b] The average sizes of supported particles determined by HRTEM.
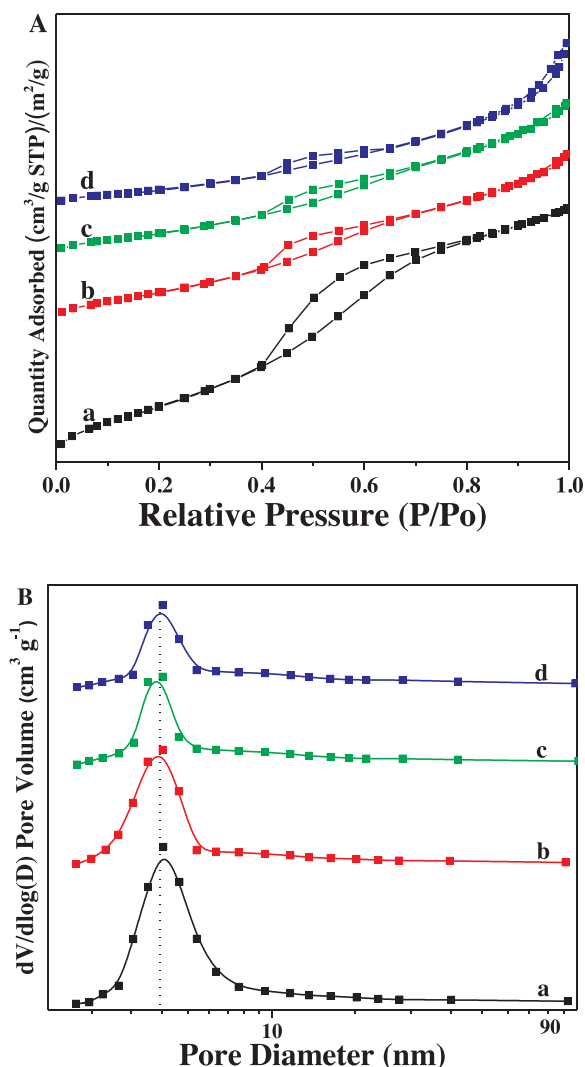[c] The actual content determined by ICP-OES.

Fig. 4. Nitrogen adsorption-desorption isotherms (A) and pore size distribution curves (B) of CZ support and 3DOMM materials. (a) mesoporous CZ support; (b) 3DOMM CZ support; (c) PdAu/3DOMM-CZ; (d) PdAu@CeO$_2$/3DOMM-CZ.
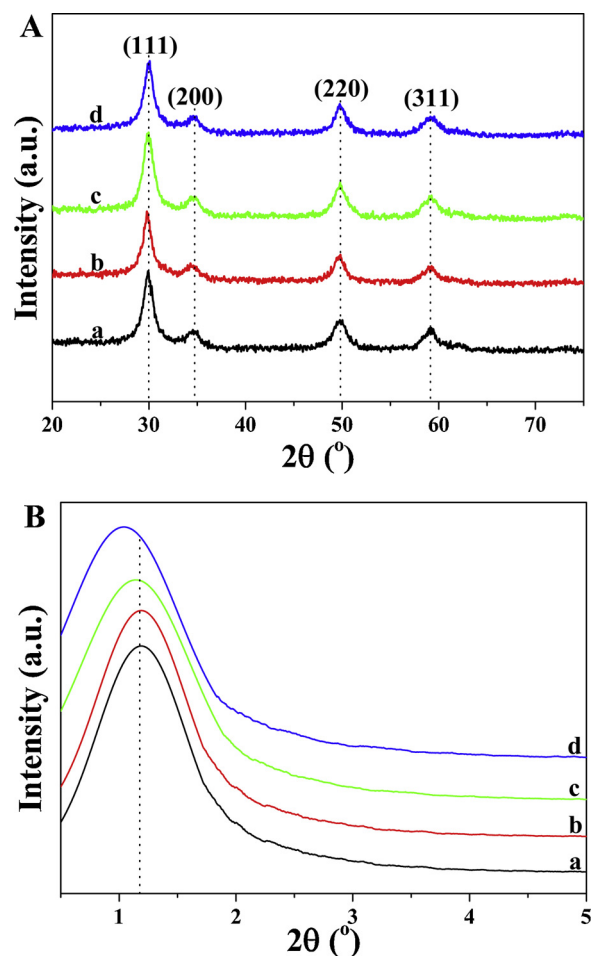

Fig. 5. Wide-angle (A) and small-angle (B) XRD patterns of CZ support and 3DOMM materials. (a) mesoporous CZ support; (b) 3DOMM CZ support; (c) PdAu/3DOMM-CZ and (d) PdAu@CeO$_2$/3DOMM-CZ.

3.4. N$_2$ adsorption-desorption measurements

Fig. 4 exhibits the representative N$_2$ adsorption-desorption isotherms and mesopore size distribution curves of typical catalysts. As displayed in Fig. 4A, the ordered mesoporous CZ support as the reference exhibits clearly the H4 hysteresis loop in the range of P/P$_0$ = 0.4-0.8. It is worth noted that 3DOMM CZ, PdAu/3DOMM-CZ and PdAu@CeO$_2$/3DOMM-CZ catalysts also show the similar hysteresis loop, indicating that ordered mesoporous structure certainly existed in the prepared catalysts. Meanwhile, all 3DOMM catalysts have a H3 hysteresis loop in the range of P/P$_0$ = 0.8 ~ 1.0, which is associated with 3D ordered macroporous framework. It indicates the formation of the hierarchical pore structure, and the macroporous structure is rarely destroyed with the formation of mesoporous structure.

Fig. 4B shows the pore size distribution curves of mesoporous CZ support and 3DOMM catalysts. The ordered mesoporous CZ support possesses narrow pore size distribution, and the mesopore size is about 4.9 nm in Table 1. For 3DOMM CZ support, the peak intensity of curves declines slightly compared with that of ordered mesoporous CZ, and the mesopore size is about 4.8 nm. After introduction of supported PdAu and PdAu@CeO$_2$ core-shell NPs, the peak intensities of curves further descent and the mesopore sizes decrease to 4.8 and 4.7 nm, respectively Table 1. It indicates that the part of PdAu@CeO$_2$ core-shell NPs have

entered into the ordered mesopores. In a word, 3DOMM catalysts have both 3D ordered hierarchical structure of meso-macropores. The plenty of ordered mesopores dispersed on the walls of macropores can increase specific surface area dramatically. It is beneficial to promote contact efficiency of catalysts-reactants and increase the surface density of active sites for soot oxidation.

3.5. XRD patterns

Fig. 5 showed the wide-angle and low-angle X-ray diffraction patterns of ordered mesoporous CZ and 3DOMM catalysts. As shown in Fig. 5A, the diffraction peaks located at 30.0, 34.7, 50.0 and 59.3° can be indexed to (111), (200), (220) and (311) crystal faces of Ce$_{0.3}$Zr$_{0.7}$O$_2$ composite oxide with the face-centered cubic (FCC) fluorite structure, respectively. The positions of diffraction peaks shift to higher angle of 2θ compared with those of CeO$_2$ because of Zr cations doping into the crystal lattice of CeO$_2$ [30]. After introduction of supported PdAu and PdAu@CeO$_2$ NPs, no new peaks were observed, indicating that PdAu or PdAu@CeO$_2$ NPs are highly dispersed on the surface of 3DOMM CZ and have not changed the crystal structure of CZ support. The low-angle XRD patterns of CZ support and typical 3DOMM catalysts are shown in Fig. 5B. The samples show the strong diffraction peak of 2θ at 0.9–1.1°, which is assigned to (100) crystal face of the typical 2D hexagonal (p6mm) style of ordered mesoporous structure. It is the direct proof to confirm ordered mesoporous nanostructure existing on the wall of 3D ordered macoporous oxide. For the catalysts of supported PdAu NPs, the position of low-angle diffraction peak has not changed obviously,
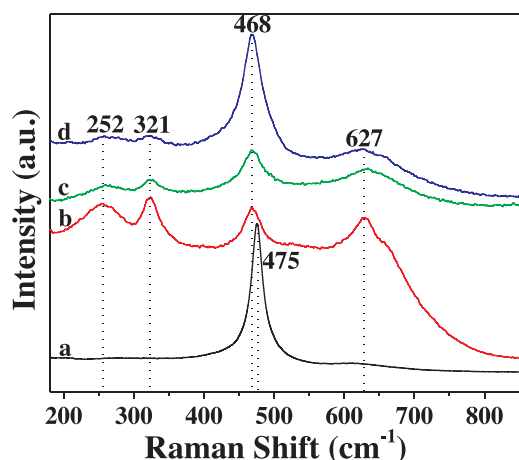
Fig. 6. Raman spectra of 3DOMM materials and contrast sample. (a) Pure phase CeO$_2$; (b) 3DOMM CZ; (c) PdAu/3DOMM-CZ; (d) PdAu@CeO$_2$/3DOMM-CZ.

indicating that the supported PdAu NPs on the inner wall of 3DOMM oxides have not destroyed the ordered mesopore structure. After introduction of supported PdAu@CeO$_2$ core-shell NPs, the position of low-angle diffraction peak shifts to low angle direction, indicating that the porosity and ordering of mesoporous structure on the inner wall of 3DOMM-CZ support decrease. It is attributed to that some PdAu@CeO$_2$ core-shell nanoparticles enter the mesopore, which is in accord with the results of N$_2$ adsorption-desorption and TEM images.

3.6. Raman spectra

For getting the information of M–O bond arrangement and surface lattice defects dominated by lattice oxygen vibrations, [47] the Raman spectra were applied to further research the surface structure of

catalysts with the excitation wavelength of 532 nm. To assure the homogeneity of catalyst, every sample was collected several different points among the wide zone to obtain the Raman spectra. All catalysts show a good homogeneity. Fig. 6 shows the Raman spectra of typical 3DOMM CZ, PdAu/3DOMM-CZ and PdAu@CeO$_2$/3DOMM-CZ catalysts. Pure phase CeO$_2$ is also exhibited in this figure as a contrast sample. The symbolic band of CeO$_2$ centered at 475 cm^{-1} is attributed to the F$_{2g}$ Raman-active vibration of the oxygen atoms around Ce cations in the fluorite lattice, which is the represent peak of CeO$_2$. As for 3DOMM CZ support, the symbol peak corresponding to CeO$_2$ shifts to 468 cm^{-1} due to the lattice deformation induced by the substitution of Ce cations with Zr cations. In addition, the extra band appears at around 321 cm^{-1} can be associated with the introduction of Zr ions into their original fluorite lattice position and existence of tetragonal phase in Ce-Zr oxide. [48] And the Raman band centered at 627 cm^{-1} is assigned to the double degeneration into longitudinal optical mode of CZ oxide, which is related to the formation of surface oxygen vacancies [49,50]. After introduction of supported active sites, the position of Raman peaks does not change obviously, while the peak strength varies with changing the structure of supported nanoparticles. PdAu/3DOMM-CZ catalyst with binary alloy NPs exhibits higher peak at 468 cm^{-1} than CZ support, indicating that the strong metal-oxides interaction activates effectively the Ce-O bond at the interface between PdAu NPs and Ce-Zr-O oxide. It is attributed to the surface enrichment of Ce elements at the interface between PdAu nanoaprticles and Ce$_x$Zr$_{1-x}$O$_2$ solid solution, which derives from the induced effect of strong metal/oxide interactions [45]. The phenomenon is quite favorable for enhancing the oxygen transformation during the reaction process. Additionally, it is meaningful to cover the PdAu NPs with the CeO$_2$ oxide shell for increasing the PdAu-CeO$_2$ interface area and thermostability of PdAu NPs. The Raman spectra of PdAu@CeO$_2$/3DOMM-CZ catalyst exhibits clearly a strong peak located at 468 cm^{-1}, which is similar to the curve of pure phase CeO$_2$ oxide. Meanwhile, the other weak peaks are matched with the CZ support. The results further demonstrate that
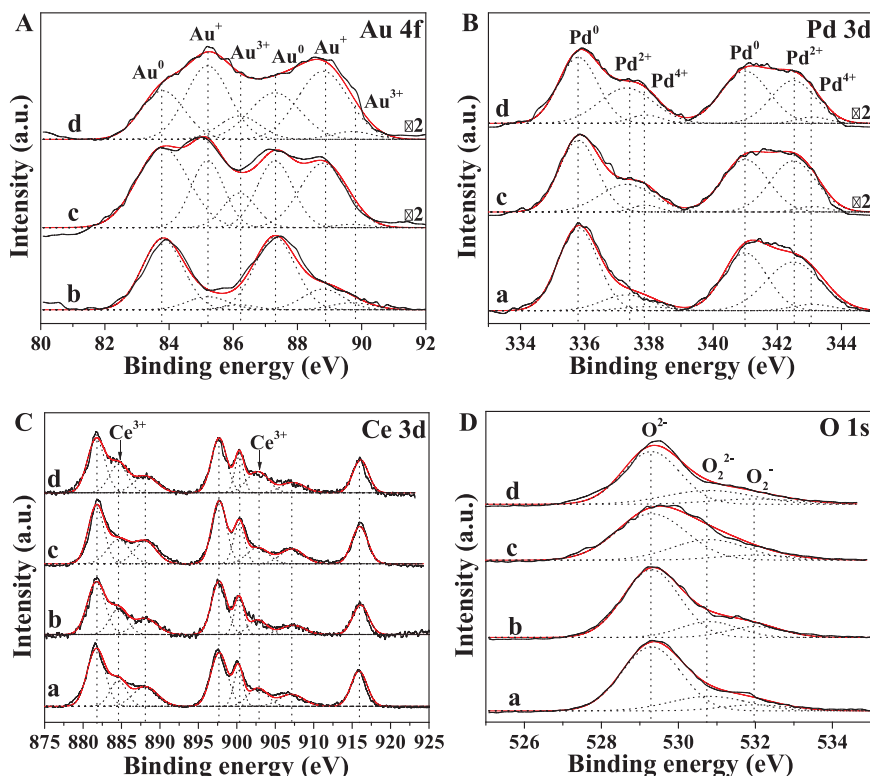

Fig. 7. XPS patterns of Au 4f (A), Pd 3d (B), Ce 3d (C) and O 1s (D) over Pd/3DOMM-CZ (a), Au/3DOMM-CZ (b), PdAu/3DOMM-CZ (c) and PdAu@CeO$_2$/3DOMM–CZ (d) catalysts.

Table 2

Surface composition and oxidation state of Pd (3d), Au (4f) and O (1s) species over 3DOMM catalysts derived from XPS analyses.

Catalysts	Au species (%)				Pd species (%)				Ce species (%)			O species (%)			
(3DOMM)	$Au°$	Au^+	Au^{3+}	R^a	$Pd°$	Pd^{2+}	Pd^{4+}	R^b	Ce^{3+}	Ce^{4+}	R^c	O^{2-}	O_2^{2-}	O_2^-	R^d
Pd/CZ	–	–	–	–	60.2	35.2	4.6	0.662	17.7	82.3	0.215	71.1	21.2	7.7	0.406
Au/CZ	76.3	17.9	5.8	0.310	–	–	–	–	18.4	81.6	0.225	71.5	17.0	11.5	0.399
PdAu/CZ	52.5	38.4	9.1	0.906	55.4	40.9	3.7	0.805	19.2	80.8	0.238	62.8	29.6	7.6	0.592
PdAu@CeO$_2$/CZ	36.1	53.7	10.2	1.769	54.4	40.7	4.9	0.838	23.1	76.9	0.300	64.4	25.6	10.0	0.553

[a] The Au species ratio of $(Au^+ + Au^{3+})/Au°$.

[b] The Pd species ratio of $(Pd^{2+} + Pd^{4+})/Pd°$.

[c] The Ce species ratio of Ce^{3+}/Ce^{4+}.

[d] Determined by the oxygen species ratio of the absorbed oxygen $(O_2^- + O_2^{2-})$ to lattice oxygen (O^{2-}).

there is a certain CeO$_2$ oxide shell existing on the outermost surface of catalysts. And the core-shell structure enhances the SMSI effect obviously by increasing interface areas between PdAu NPs and Ce-based oxides. The SMSI effect can activate Ce-O bond directly and increase the surface density of active oxygen species in the reaction system. Thus, the redox property of the catalysts with core-shell nanostructure can be improved accordingly.

3.7. XPS analysis

XPS analyses were used to obtain the information about the compositions and the charge states of surface elements and adsorbed species over the catalysts. The activated oxygen capability of catalyst affects closely the catalytic performance for deep catalytic oxidation [51]. The deconvolution results of Au 4f, Pd 3d, Ce 3d and O 1s XPS for the typical Pd/3DOMM-CZ, Au/3DOMM-CZ, PdAu/3DOMM-CZ and PdAu@CeO$_2$/3DOMM-CZ catalysts were shown in Fig. 7 and Table 2. Fig. 7A shows the Au 4f XPS of the catalysts. There are both metallic and ionic Au species presented in the catalysts. The binding energies pairs centered at about 83.8 and 87.3 eV, 85.2 and 88.8 eV, 86.2 and 89.7 eV can be assigned to $Au°$, Au^+ and Au^{3+} species, respectively. As shown in Table 2, for the 3DOMM Au/CZ catalyst, the metallic state of Au species is predominant (76.3%), and the ratio (R^a) of $(Au^+ + Au^{3+})$ to $Au°$ species is only 0.310. However, after introduction of Pd and CeO$_2$, the ionic state of Au species increases obviously with the formation of PdAu alloy or PdAu@CeO$_2$ core-shell NPs in the catalysts. The values of R^a also increase to 0.906 and 1.769 for PdAu/3DOMM-CZ and PdAu@CeO$_2$/3DOMM-CZ catalysts, respectively. It suggests that the increasing Au$^{\delta+}$ species can produce more active oxygen species due to the electron transfer from noble metal cores to interface at metal-support.

As shown in Fig. 7B, the results of Pd 3d XPS are similar to those of Au 4f. The pairs of binding energies located at 335.8 and 341.0 eV, 337.3 and 342.5 eV, 337.9 and 343.1 eV are assigned to $Pd°$, Pd^{2+} and Pd^{4+} species, respectively. The percent of $Pd°$ species in Pd/3DOMM-CZ catalyst is 60.2%, and the species ratio (R^b) of $(Pd^{2+} + Pd^{4+})$ to $Pd°$ is about 0.662. Meanwhile, the R^b values of PdAu/3DOMM-CZ and PdAu@CeO$_2$/3DOMM-CZ catalysts increase to 0.805 and 0.838, respectively. It indicates that the metallic Pd species transform into ionic Pd^{2+} species. The increasing content of metal cations induces the formation of active oxygen species at the interface between PdAu NPs and Ce-Zr oxide. It is deduced that the decrease in the d-electron density of the Pd elements generates the increasing amount of surface active oxygen species.

To confirm the electron transfer between metal cores and oxide shells, Fig. 7C shows the deconvolution results of Ce 3d XPS. The binding energies centered at 881.7, 884.6, 888.1 and 897.7 eV are assigned to Ce 3d$_{5/2}$; and the binding energies centered at 900.3, 902.7, 907.3 and 916.1 eV are belonged to Ce 3d$_{3/2}$. Among all the peaks, the XPS peaks centered at 884.6 and 902.7 eV represent the Ce^{3+} species while others represent the Ce^{4+} species. As shown in Table 2, with the

formation of PdAu alloy or PdAu@CeO$_2$ core-shell NPs, the percents of Ce^{3+} species increase to 19.2% and 23.1% for 3DOMM PdAu/CZ and PdAu@CeO$_2$/CZ catalysts, respectively. 3DOMM PdAu@CeO$_2$/CZ catalyst with optimal PdAu-CeO$_2$ interface area possesses the largest ratio (R^c) of Ce^{3+}/Ce^{4+} species (0.300), indicating that the electron transfer from metal core to oxide shell induce more lattice Ce^{4+} transform into activated Ce^{3+} cations. The increasing content of Ce^{3+} species could lead to the increase of oxygen vacancies on the surface of catalyst. Furthermore, the oxygen vacancies activate more gaseous oxygen to generate active oxygen species for improving catalytic performance of soot oxidation.

Fig. 7D exhibits the existence state of oxygen species among all the catalysts, which is extreme significant to the soot oxidation reaction. The binding energies of O 1 s centered at 529.3, 530.8 and 532.0 eV are belonged to lattice oxygen (O^{2-}) species and active oxygen (O_2^{2-} and O_2-) species, respectively. It is generally accepted that O_2^{2-} and O_2- species are mainly active species for soot oxidation. For Pd/3DOMM-CZ and Au/3DOMM-CZ catalysts, the percent of lattice O^{2-} species is more than 70%, and the ratios (R^d) of $(O_2$- $+ O_2^{2-})$ to O^{2-} species are 0.406 and 0.399, respectively. It can be noted that the percent of active oxygen species increases remarkably for the 3DOMM PdAu/CZ and PdAu@CeO$_2$/CZ catalysts. Specially, the percent of O_2^{2-} species over 3DOMM PdAu/CZ catalyst is 29.6% and its R^d value is the largest (0.592). The percent of O^{2-} species increases slightly to 64.4% for 3DOMM PdAu@CeO$_2$/CZ catalyst due to the coverage of CeO$_2$ on the catalyst surface. The results indicate that the supported PdAu alloy or PdAu@CeO$_2$ core-shell sites are all benefit for promoting the formation of surface active oxygen species. The catalyst with core-shell nanostructure shows the high density of active oxygen species, which should be matched with the better catalytic performance. It is rooted in that the core-shell nanostructure maximizes the contact area between binary noble metal core and CeO$_2$ oxide shell, and promotes the SMSI effect attributed to the induced electrons transfer from metal core to outmost shell at the interface [52]. The increasing metal cations and active oxygen species could activate the gaseous reactants dramatically to enhance the reaction activity for soot catalytic oxidation.

3.8. H$_2$-TPR tests

The catalytic performance for heterogeneous deep oxidation reaction is strongly related to their redox property. H$_2$-TPR experiment is a widely-applied technology to obtain the oxidation proprety of active oxygen species. The results of H$_2$-TPR tests can reveal the reducibility of metallic ions of high valence to low valence or metallic atoms, and the potential to remove or take up oxygen, i.e., the mobility of the lattice oxygen (O^{2-}). The effects of supported PdAu or PdAu@CeO$_2$ NPs on redox property of surface oxygen species were investigated by the temperature and intensity of reduction peak (T_{red}), and the results are exhibited in Fig. 8. 3DOMM CZ oxide possesses two reduction peaks in the range of 400–800 °C. The reduction peak located at 487 °C is associated with the reduction of outermost layers of Ce^{4+} to Ce^{3+}. And the
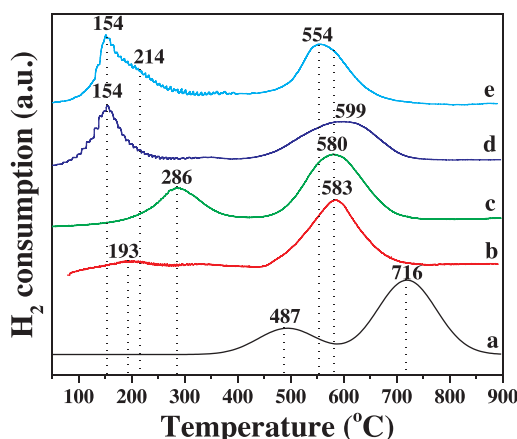
Fig. 8. The H_2-TPR profiles of 3DOMM catalysts. (a) 3DOMM CZ support; (b) Pd/3DOMM-CZ; (c) Au/3DOMM-CZ; (d) PdAu/3DOMM-CZ and (e) PdAu@CeO$_2$/3DOMM-CZ catalysts.

peak located at 716 °C is assigned to the reduction of bulk Ce^{4+} species and lattice oxygen in inner layer of CZ oxide. The lower T_{red} is, the better activity of surface oxygen species is. Compared with CZ support, Pd/3DOMM-CZ catalyst exhibits a low temperature reduction peak centered at 193 °C which is assigned to the reduction of active oxygen (O_2^{2-}, O_2-) species derived from adsorption and activation of supported Pd NPs. [53] Meanwhile, the peak of bulk reduction at 583 °C is much lower than that of CZ oxide, indicating that the strong metal-support interaction between CZ oxide and supported Pd NPs improve their redox property. For Au/3DOMM-CZ catalyst, the reduction peak at 286 °C is assigned to the reduction processes of active oxygen species adsorbed on Au NPs [54]. The peak corresponding to bulk reduction at 580 °C is also lower than that of CZ oxide.

It is interesting to find that the catalysts of supported PdAu alloy or PdAu@CeO$_2$ core-shell NPs show better redox property than Pd/3DOMM-CZ and Au/3DOMM-CZ catalysts. The reduction temperature of active oxygen species decreases to 154 °C because of the synergistic effect between noble metal components of Au and Pd at atomic scale. [40] For PdAu@CeO$_2$/3DOMM-CZ catalyst, there is one extra shoulder peak centered at 214 °C, which is associated with the oxygen species derived from the interaction between PdAu core and CeO$_2$ shell. [29] The additional redox capacity at low temperature is very important for improving the catalytic performance of catalyst. In addition, the peak temperature associated with bulk reduction decreases to 554 °C for PdAu@CeO$_2$/3DOMM-CZ catalyst. It indicates that the core-shell nanostructure is favorable for improving the surface density of active sites and activating lattice oxygen because of the increasing interface area between the PdAu binary alloy core and CeO$_2$ shell. The interactions derived from the special core-shell nanostructure are further beneficial for catalytic soot oxidation. Additionally, to reveal the intrinsic oxygen species density of the catalysts, a series of soot-TPR measurements were also conducted and the results are shown in Fig. S4. The soot-TPR results show that supported noble metal components can improve the intrinsic oxygen species density due to strong activation ability. PdAu@CeO$_2$/3DOMM-CZ catalyst possesses the largest density of intrinsic oxygen species because of the enhanced SMSI effect for activating lattice oxygen in oxide shell.

3.9. Catalytic activity for soot oxidation

The activities and selectivities of 3DOMM CZ support and supported AuPd and AuPd@CeO$_2$ core-shell NP catalysts for soot oxidation were evaluated by TPO reaction under the conditions of soot-catalyst loose contact in the presence of O_2 (5 vol %), NO (0.2 vol %) and H_2O (5 vol %) balanced with Ar, and the results are listed in Table 3 and Fig. 9.

Compared with the result of soot oxidation without catalyst (T_{50} = 589 °C), 3DOMM CZ support shows high catalytic performance for soot oxidation, i.e., the valves of T_{10}, T_{50} and T_{90} are 356, 459, and 514 °C, respectively. After introduction of supported noble metal NPs, the catalytic activities of all the catalysts were further improved, which derive from the enhanced adsorption and activation capacities for gaseous reactants. PdAu/3DOMM-CZ catalyst possesses higher catalytic performance for soot oxidation in comparison with supported single metal catalysts (Pd/3DOMM-CZ and Au/3DOMM-CZ), and its T_{10}, T_{50} and T_{90} are 292, 379 and 426 °C, respectively. It indicates that there is a synergistic effect between two effective components to improve redox capacity of catalysts, which is matched with the H_2-TPR results. In practical application, the catalytic activity for soot oxidation at low temperature (T_{10} value) is more important than the values of T_{50} and T_{90}. After the introduction of CeO$_2$ shell to form core-shell nanostructure active sites, the T_{10} value of PdAu@CeO$_2$/3DOMM-CZ catalyst decreases to 276 °C, which is benefit for removing soot particles at relatively low temperature. The catalytic performance at low temperature is closely associated with the density of active oxygen species. The activity of PdAu@CeO$_2$/3DOMM-CZ catalyst roots in the increasing density of active sites because of the optimal interfaces area between PdAu binary alloy NPs and CeO$_2$ shell. As shown in Table 3, the selectivity of CO_2 product for 3DOMM CZ support is about 75.4%. After introduction of noble metal active components supported on the 3DOMM CZ, the selectivities of CO_2 product increase to nearly 100%, indicating that CO pollutant derived from vehicle exhaust can be removed immediately. All results were obtained in the presence of 5 vol % H_2O, indicating that CeO$_2$ shell has an effective protection for metal core form inhibition of H_2O. In order to investigate the relationship between NO$_2$ variations and catalytic performance, the NO$_2$ production curves were added into the soot conversion profiles. As shown in Fig. 9A–E, the soot conversion is closely related to the NO$_2$ production, indicating that the ability of the catalyst to oxidize NO is very important for soot catalytic oxidation. For 3DOMM CZ support (Fig. 9A), the peak concentration of NO$_2$ is about 200 ppm and occurs at 453 °C. While for PdAu@CeO$_2$/3DOMM-CZ catalyst with best catalytic performance (Fig. 9E), the peak concentration of NO$_2$ increases to 450 ppm and the temperature decreases to 371 °C. The results are quite in favor of the points that NO$_2$-assited mechanism is the main reaction pathway for catalytic soot oxidation and better catalytic activity for NO can promote soot oxidation.

In addition, PdAu@CeO$_2$ core-shell nanostructure can also improve the sintering resistance of PdAu NPs in the reaction process of soot oxidation. It is very important to catalysts in practical application. Fig. S5 shows the catalytic activities of PdAu/3DOMM-CZ and PdAu@CeO$_2$/3DOMM-CZ catalysts during the consecutive testing processes. The T_{50} values of PdAu/3DOMM-CZ catalyst increases from 379 (first-cycle) to 393 °C (fifth-cycle), while PdAu@CeO$_2$/3DOMM-CZ catalyst still remains high catalytic performance in five cycles of TPO tests, i.e., its values of T_{10}, T_{50} and T_{90} are still 278, 366 and 407 °C for fifth time test, respectively. As shown in Fig. S6 of TEM images, the ordered hierarchical meso-macroporous structures of PdAu@CeO$_2$/3DOMM-CZ catalyst used for five TPO cycles keep perfectly, and supported PdAu@CeO$_2$ NPs are still highly dispersed on the inner wall of CZ supports. The average size of PdAu@CeO$_2$ core-shell NPs is 4.1 nm, indicating that the core-shell nanostructure effectively prevents nanoparticle to agglomerate during the process of soot oxidation. However, after the hydrothermal treatment at 900 °C for 4 h, the catalytic activity of PdAu@CeO$_2$/3DOMM-CZ catalyst decreases slightly (Fig. S10), which is attributed to the decreasing ordering of mesoporous structure and the increasing sizes of supported PdAu@CeO$_2$ core-shell NPs (Fig. S11). Thus, it is still a great challenge to keep the ordering of mesoporous structure and inhibition sintering of PdAu@CeO$_2$ core-shell nanoparticles at relatively high temperature in the future.

The intrinsic activity of catalyst is generally evaluated by TOF, which is defined as the ratio of the reaction rate (R) to the active oxygen

Table 3

The catalytic performance, selectivity, oxygen vacancy density (O_v), reaction rate (R) and TOF_{Ov} value of 3DOMM catalysts for soot oxidation under the conditions of loose contact in the presence of O_2 (5 vol %), NO (0.2 vol %) and H_2O (5 vol %) balanced with Ar.

Catalysts (3DOMM)	T_{10} (°C)	T_{50} (°C)	T_{90} (°C)	$S_{CO2}{}^m$ (%)	Oxygen amount (μmol g^{-1})[a]	Density of O[a] (μmol g^{-1})[b]	R (μmolg^{-1} s^{-1})[c]	TOF_{Ov} (h^{-1})[d]
Soot (without catalyst)	485	589	647	51.2	–	–	–	–
CZ support	356	459	514	75.4	27.3	54.6	0.007	0.46
Pd/CZ	336	419	472	96.6	37.4	74.8	0.026	1.25
Au/CZ	311	410	462	99.5	47.1	94.2	0.054	2.06
PdAu/CZ	292	379	426	99.6	50.0	100.0	0.063	2.27
PdAu@CeO$_2$/CZ	276	363	404	99.6	53.7	107.4	0.075	2.51

[a] Determined by isothermal anaerobic titrations experiments at 290 °C.

[b] The density of active oxygen (O_a) is equal to oxygen amount/mass (catalyst).

[c] Determined by conversion for soot combustion at 290 °C.

[d] The computational formula: $TOF_{Ov} = R/D_{Ov}$.
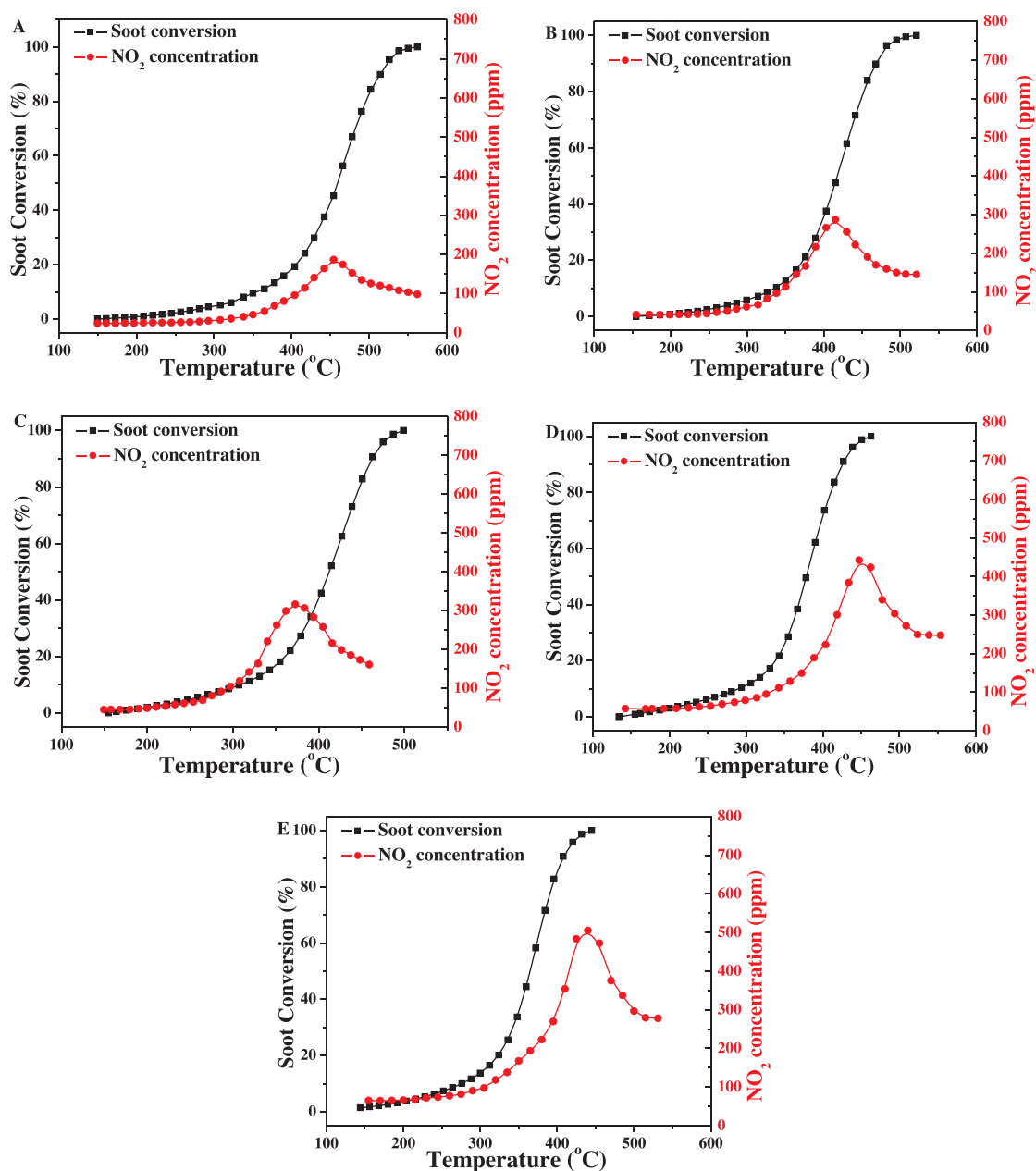

Fig. 9. The profiles of soot conversion and NO$_2$ concentration over 3DOMM materials under the conditions of soot-catalyst loose contact in the presence of O$_2$ (5 vol %), NO (0.2 vol %) and H$_2$O (5 vol %) balanced with Ar. (A) 3DOMM CZ; (B) Pd/3DOMM-CZ; (C) Au/3DOMM-CZ; (D) PdAu/3DOMM-CZ; (E) PdAu@CeO$_2$/3DOMM-CZ.

(O_a) amount. Reaction rates of all the catalysts are estimated by an isothermal oxidation reaction at 290 °C in the kinetic regime and the uniform structure of catalysts could exclude the intraparticle mass transport limitations. Amounts of active oxygen species are acquired by an isothermal anaerobic titration experiment at 290 °C. As shown in Table 3 and Fig. S7, 3DOMM CZ support exhibits the low soot oxidation rate at 290 °C, the R value is only 0.007 $\mu mol\, g^{-1}\, s^{-1}$. Supported noble metal components improve the isothermal oxidation rate obviously and the R values increase to 0.026 and 0.054 $\mu mol\, g^{-1}\, s^{-1}$ for Pd/3DOMM-CZ and Au/3DOMM-CZ catalysts, respectively. The fabricating of the binary alloy or core-shell nanostructure active sites can further promote the R value. PdAu@CeO_2/3DOMM-CZ possesses the largest R value (0.075 $\mu mol\, g^{-1}\, s^{-1}$), indicating that the PdAu@CeO_2 core-shell structure is benefit for improving the catalytic performance for soot oxidation. Fig. S8 and Table 3 show that the PdAu@CeO_2/3DOMM-CZ catalyst possesses the larger density of active oxygen (178 $\mu mol\, g^{-1}$) than other catalysts due to the enhanced SMSI effect which can activate the active oxygen (O_a) sites at oxide shell or interface to improve the value of O_a density. TOF values for all the catalysts are evaluated by the ratio of R/O_a and the results are listed in Table 3. As shown in the results, PdAu@CeO_2/3DOMM-CZ catalyst exhibits the best intrinsic activity for soot oxidation, i.e., its TOF value is the largest (2.51 h^{-1}), which is more than 5-fold increase for 3DOMM CZ oxide support (0.46 h^{-1}). Additionally, the PdAu/3DOMM-CZ with binary alloy sites possesses higher TOF value of 2.27 h^{-1} than the supported single component catalysts (Pd/3DOMM-CZ and Au/3DOMM-CZ). The results suggest that supported PdAu NPs can improve the intrinsic activity of catalyst by promoting adsorb-activate property in comparison with those of supported single noble metal NPs, and the synergetic effect of Pd-Au-CeO_2 ternary components in PdAu@CeO_2 core-shell nanostructure can further enhance catalytic performance for soot oxidation.

To verify the influence of NO, SO_2 and H_2O on the catalytic performance for soot oxidation, the catalytic activities of PdAu@CeO_2/3DOMM-CZ catalyst under different gaseous conditions were investigated. As the results shown in Fig. S9, in the presence of only O_2(5 vol %) and H_2O(5 vol %) without assist of NO condition, the catalytic performance decreases remarkably among the reaction temperature range. The T_{10} and T_{50} values decrease to 400 and 460 °C at the reaction atmosphere without containing NO. In the presence of NO (0.05 vol %), O_2 (5 vol %) and H_2O (5 vol %), the catalytic performance for soot oxidation at low temperature (T_{10} = 324 °C) decrease dramatically compared with that of 0.2 vol % NO atmosphere (T_{10} = 276 °C). However, as the temperature rising up, the effect of NO concentration on catalytic activity for soot oxidation weakens slightly. The T_{50} values are 369 °C (0.05 vol % NO) and 363 °C (0.2 vol % NO), respectively. It confirms that the role of NO is very important to promote the catalytic soot oxidation process. The NO/NO_2 cycles can transform the reaction of gas (O_2)-solid (catalyst)-solid (soot) into solid (catalyst)-gas (NO_2)-solid (soot) style even at the extreme low concentration. After the introduction of both NO(0.2 vol %), O_2(5 vol %), H_2O(5 vol %) and SO_2(0.02 vol %), the T_{50} value decreases to 385 °C and PdAu@CeO_2/3DOMM-CZ catalyst still remains high catalytic performance, indicating that the CeO_2 shell possesses good SO_2 tolerance. It is attributed to that CeO_2 oxide has appropriate acidity to inhibit the SO_2 adsorption. The results reveal that core-shell nanocatalysts have excellent resistance in practical application of emission reduction.

4. Discussions

4.1. The influence of 3DOMM and core-shell nanostructures on catalytic activity for soot oxidation

Diesel soot catalytic oxidation is a typical heterogeneous catalysis reaction occurring at the interface of solid (soot)-solid (catalyst)-gas (O_2) three phases. The performance for catalytic soot oxidation is closely related to the contact efficiency of catalyst-reactants and

adsorption-activation properties for gaseous reactants. For the fabrication of 3DOMM nanostructure via the EISA-CCT method, the structures of highly ordered macroporous and mesoporous framework enhance the contact efficiency of soot-catalyst effectively. Ordered macropores decrease transmission resistance of the reactants, and thus the contact efficiency between catalysts and solid reactants (soot) can be improved remarkably. And the plenty of ordered mesopores increase the specific surface area, which is quite beneficial to enhance adsorption and activation capacities for the gaseous reactants. During the process of "soot-flow" through hierarchical porous nanostructure with the assist of gas reactants, the contact efficiency of catalyst-soot and catalyst-gas would be improved dramatically. Meanwhile, the hierarchical nanostructure can reduce the migration distance of NO_2 from active sites to soot particles and further enhance oxidation efficiency of soot particles. Thus, the catalytic activity could be improved whatever the reaction pathway is direct or indirect. [30]

The well-known NO_2-assited mechanism is the main reaction pathway for catalytic soot oxidation. Fig. S9 shows that NO_2 derived from fast oxidation of NO in diesel exhaust can be an efficient mobile oxidizing species, which accesses soot particles easily and causes light-off of soot in an appropriate temperature range because of the higher oxidation capacity of NO_2 in comparison with O_2. Thus, it is very crucial to promote the activation ability of catalysts for gaseous reactants (O_2 and NO). Increasing the density of active sites and enhancing the SMSI effect could be two efficient means. NO-TPO measurements were conducted on the online Fourier transform infrared spectroscopy to investigate the activation property of the 3DOMM catalysts for gaseous reactants. As shown in Fig. 10, 3DOMM CZ support exhibits lower NO_2 concentration compared with those of 3DOMM CZ-supported active NP catalysts. The temperature of peak locates at 380 °C is much higher than those of supported noble metal catalysts. After supported active components on the inner surface of CZ support, the produced NO_2 concentrations increase and the peak temperatures decrease obviously. It is noted that the PdAu binary component catalysts have the higher NO_2 concentration than both single component catalysts, indicating that the synergistic effect between Au and Pd components is benefit for activating NO and O_2. Among all as-prepared catalysts, the PdAu@CeO_2/3DOMM-CZ catalyst possesses the best activation capacity for NO and the peak temperature decreases to about 320 °C, indicating that the optimal interface areas between alloy core and oxide shell can increase the density of active oxygen species. The results confirm that the noble metal active components and core-shell nanostructure are benefit for improving activation property of catalysts for gaseous reactants. NO_2 concentration plays a crucial role in the catalytic oxidation process and the rate of soot oxidation is certainly linked to the NO_2 production and then to the ability of catalyst to oxidize NO.
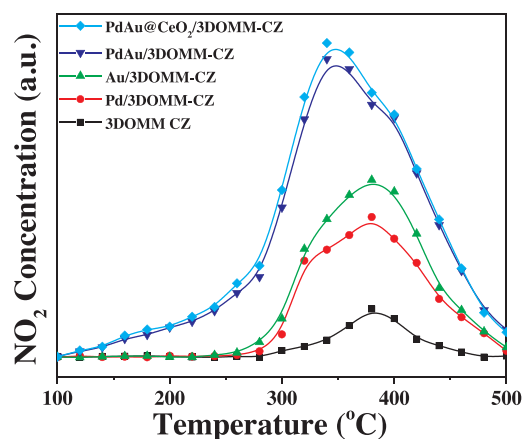

Fig. 10. The NO_2 concentration curves of NO temperature programmed oxidation (NO-TPO) over 3DOMM materials.

In addition, the PdAu binary alloy nanoparticles tune the atomic-scale characteristics, which induce significant changes in the electronic structure and catalytic properties. [55] On the other hand, CeO_2 shell not only protects the PdAu binary alloy core to improve stability, but also enhances the SMSI effect to produce more active oxygen species. Herein, the supported $PdAu@CeO_2$ core-shell NPs have excellent durability and activation capacity for the gaseous reactants. $PdAu@CeO_2$/3DOMM-CZ catalyst, which combines with 3D ordered hierarchical mesoporous-macroporous framework and $PdAu@CeO_2$ core-shell nanostructure, exhibits super catalytic performance for soot oxidation and strong structure-dependent relationship. It is an appropriate system to further research complex heterogeneous catalytic reaction containing solid or large molecule reactants.

4.2. The catalytic mechanism of PdAu@CeO₂/3DOMM-CZ catalyst for soot oxidation

To in-depth expose the reaction mechanism of $PdAu@CeO_2$/3DOMM-CZ catalyst, in-situ Raman measurements were conducted on the inVia Reflex-Renishaw spectrometer with the He-Gd laser source whose excitation wavelength is 532 nm. The reaction atmosphere consists of 5% O_2 and 0.2% NO balanced with He which is similar to the activity testing process. The variation of intermediate species was observed at the reaction temperature ranges from 50 to 450 °C. For comparison, the typical 3DOMM CZ and PdAu/3DOMM-CZ samples were also included. As shown in Fig. 11A, 3DOMM CZ support exhibits a weak Raman band at 1053 cm^{-1}, which is associated with the surface adsorbed oxygen species (O_2-). [56] With rising of the temperature, the peak decreases gradually and disappears completely at about 350 °C, indicating that the O_2- species on the surface of CZ support is not stable. Meanwhile, the Raman band centered at 1196 cm^{-1} is assigned to the

activated Ce-O bond, the intensity of the peak appears with the increasing of temperature. [57] It is attributed to the gaseous reactants transform into NO_2 and then reacts with Ce cations.

Fig. 11B shows that, after supported PdAu alloy NPs, the intensity of peak at 1053 cm^{-1} is higher than CZ oxide support, and disappears at higher temperature (> 350 °C). It indicates that the supported binary noble metal components are favorable for forming active oxygen species and keep them stable among the reaction temperature range. In addition, the Raman peak at 1196 cm^{-1} appears at much lower temperature, indicating that PdAu alloy sites also benefit for activation of nitric oxide at relatively low temperature. As shown in Fig. 11C, $PdAu@CeO_2$/3DOMM-CZ catalyst has strong peak at 1053 cm^{-1}, indicating super adsorption and activation capacity for O_2 on the $PdAu@CeO_2$ sites. However, the peak decreases with the rising of temperature while the other Raman peak at 1028 cm^{-1} associated with the active O_2^{2-} species appears gradually. [58] The O_2- species disappear almost at 450 °C but the O_2^{2-} species still exist at the high temperature. It indicates that $PdAu@CeO_2$ core-shell nanostructure possesses the ability to promote the density of active oxygen species (O_2^{2-}) for enhancing the redox capacity and thermal stability of catalysts. Another Raman peak centered at 1286 cm^{-1} is still associated with the activated Ce-O bond. The Raman bands shift from 1196 cm^{-1} to 1286 cm^{-1} just because the Ce cations in CeO_2 shell are different from that in Ce-Zr solid solution. The existence of activated Ce-O bond at low temperature further confirms the activation ability of noble metal for nitric oxide. In summary, the binary noble metal components can activate NO/O_2 to form active oxygen species at low temperature while core-shell nanostructure with the enhanced SMSI can transfer electrons from core to shell and promote the formation of active oxygen species. $PdAu@CeO_2$ core-shell active sites, combined with the binary noble metal core and the CeO_2 oxide shell, exhibit the excellent
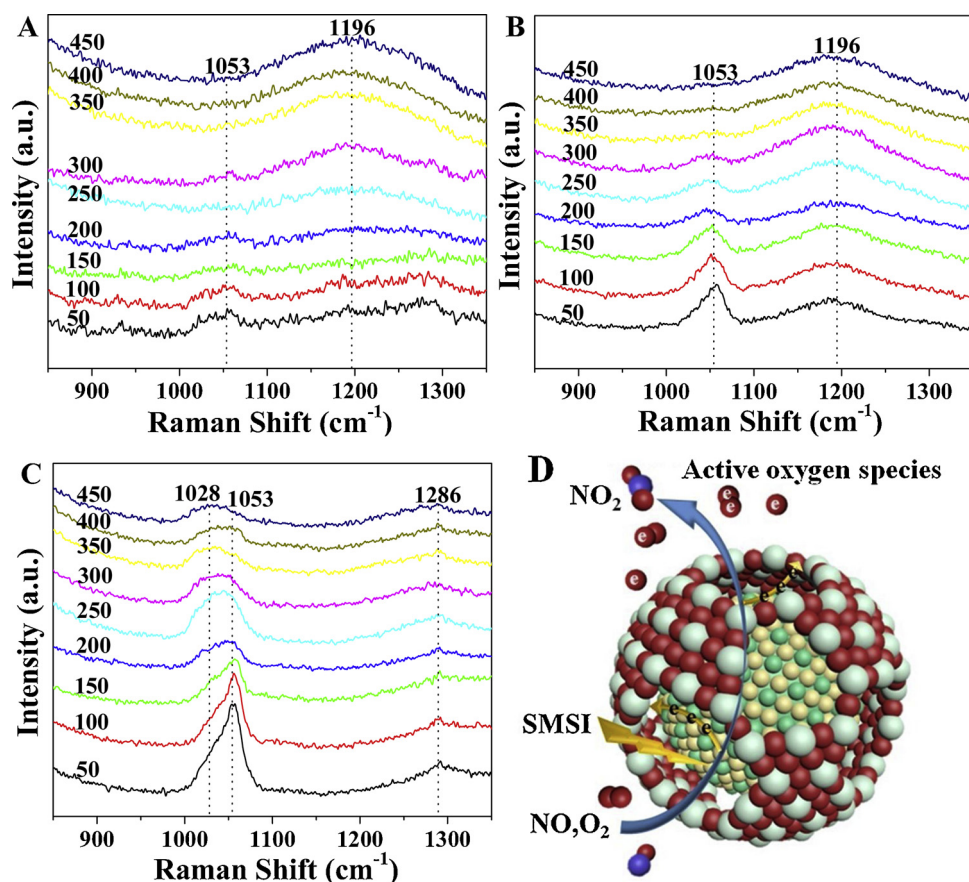

Fig. 11. In situ Raman measurements of 3DOMM CZ (A), PdAu/3DOMM-CZ (B), PdAu@CeO₂/3DOMM-CZ (C) catalysts in 5% O₂ + 2000 ppm NO + He atmosphere (total flow 50 ml min⁻¹); and catalytic mechanism of core-shell active sites (D).
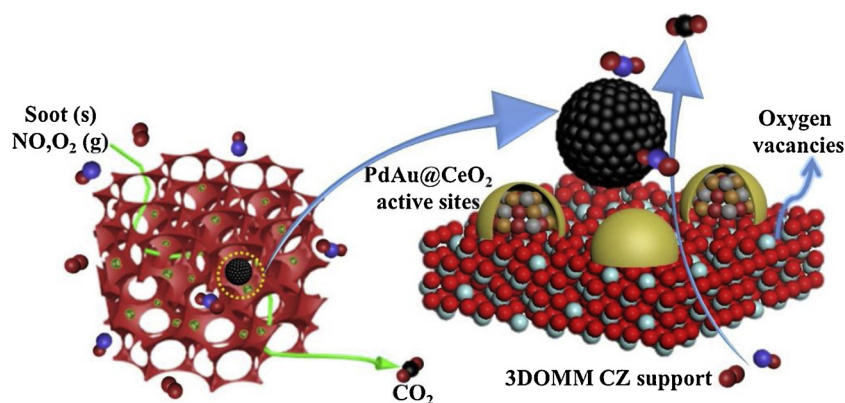
Fig. 12. Mechanism illustration of PdAu@CeO$_2$/3DOMM-CZ catalyst for soot combustion under the loose contact condition.

catalytic performance for soot combustion.

Fig. 11D shows vividly the catalytic mechanism of PdAu@CeO$_2$ core-shell NPs in the catalytic NO oxidation process. There is a strong metal-support interaction between the active components and support. The core-shell nanostrucrure increases the contact area dramatically between PdAu NP and CeO$_2$ layers, which is benefit for enhancing the SMSI effect to improve the amount of active oxygen species. There is an electron transfer process from metal core to oxide shell, where the decreasing d- or f-electron density of metal core may lead to an increase in the density of surface oxygen vacancies and active oxygen species. [59] When the gaseous reactants (NO and O$_2$) are adsorbed by the PdAu@CeO$_2$ core-shell active sites, the negative oxygen ions and oxygen vacancies react with them to form NO$_2$ and active oxygen species with excellent oxidation capacity. Therefore, the catalytic performance for soot oxidation can be promoted obviously.

By summarizing all the results, a possible reaction mechanism was supposed and shown in Fig. 12. The excellent catalytic performance of PdAu@CeO$_2$/3DOMM-CZ catalyst rooted in two aspects: Firstly, the ordered hierarchical porous nanostructure improves the contact efficiency between catalysts and reactants. 3DOMM CZ support not only promotes the mass transfer of reactants (soot and gaseous reactants) in the inner space of catalyst, but also offers enhanced surface area to disperse active sites adequately. Secondly, the core-shell nanostructure active sites and oxide shell/support show the enhanced SMSI effect because of the increasing interfaces area between PdAu alloy cores and CeO$_2$ shells. It is very important to improve density of oxygen vacancies and redox property in reaction process. The active oxygen species derived from oxygen vacancies and PdAu@CeO$_2$ core-shell sites are favorable for oxidizing soot particles and NO to CO$_2$ and NO$_2$, and the step of NO oxidation to NO$_2$ is the determining step for soot oxidation in NO$_2$-assisted catalytic mechanism. Therefore, PdAu@CeO$_2$/3DOMM-CZ catalyst, which combines of both advantages of good contact efficiency between catalysts and reactants (soot, NO and O$_2$) and the synergetic effect of Pd-Au-CeO$_2$ ternary components for oxygen activation, shows excellent catalytic activity and stability for soot oxidation.

5. Conclusions

The multifunctional catalysts of 3DOMM Ce$_{0.3}$Zr$_{0.7}$O$_2$ composite oxide supported PdAu@CeO$_2$ core-shell nanoparticles are designed and synthesized by the novel combined methods of EISA-CCT and GBMR/P methods. 3DOMM hierarchical porous materials possess both ordered macroporous framework and ordered mesoporous structure. 3D ordered macroporous framework can enhance the mass transfer of soot particles in the inner space of catalyst, and improve the contact efficiency of soot-catalyst. The mesoporous structure provides the higher surface area, which is favorable for improving surface density of active sites and increases the contact efficiency between catalyst and gaseous reactants (NO and O$_2$). The PdAu@CeO$_2$ core-shell nanostructure with

the increasing interface area between binary alloy core and CeO$_2$ shell can improve the density of active oxygen species obviously. PdAu@CeO$_2$/3DOMM-CZ catalyst, which possesses both hierarchical porous framework and core-shell nanostructure active sites, exhibits super catalytic performance and stability for soot oxidation under the conditions of soot-catalyst loose contact in the presence of O$_2$, NO and H$_2$O, i.e., its T$_{10}$, T$_{50}$, T$_{90}$ values are only 276, 363, 404 °C, respectively. Its TOF value reaches to 2.51 h^{-1} at 290 °C, which is more than 5-fold increase for 3DOMM CZ oxide support (0.46 h^{-1}). The catalytic mechanism of PdAu@CeO$_2$/3DOMM-CZ catalyst is systematic investigated. The synergetic effect of Pd-Au-CeO$_2$ ternary components can improve the density of active oxygen species, and the step of NO oxidation to NO$_2$ is the determining step for catalytic soot oxidation. The 3DOMM structure catalysts with core-shell nanostructure active sites can be also simply applied in various heterogeneous metal-oxide catalytic systems, and could illustrate a promising and efficient way to improve other catalytic reaction containing solid or large molecule reactants.

Appendix A. Supplementary data

Supplementary material related to this article can be found, in the online version, at doi:https://doi.org/10.1016/j.apcatb.2019.03.078.

References

[1] W. Shangguan, Y. Teraoka, S. Kagawa, Promotion effect of potassium on the catalytic property of CuFe$_2$O$_4$ for the simultaneous removal of NO$_x$ and diesel soot particulate, Appl. Catal. B 16 (1998) 149–154.

[2] A. Bueno-López, Diesel soot combustion ceria catalysts, Appl. Catal. B 146 (2014) 1–11.

[3] J. Oi-Uchisawa, A. Obuchi, S. Wang, T. Nanba, A. Ohi, Catalytic performance of Pt/MO$_x$ loaded over SiC-DPF for soot oxidation, Appl. Catal. B 43 (2003) 117–129.

[4] H. Wang, B. Jin, H. Wang, N. Ma, W. Liu, D. Weng, X. Wu, S. Liu, Study of Ag promoted Fe$_2$O$_3$@CeO$_2$ as superior soot oxidation catalysts: the role of Fe$_2$O$_3$ crystal plane and tandem oxygen delivery, Appl. Catal. B 237 (2018) 251–262.

[5] K. Mori, Y. Iwata, M. Yamamoto, N. Kimura, A. Miyauchi, G. Okamoto, T. Toyoshima, H. Yamashita, An efficient Cu/BaO/La$_2$O$_3$ catalyst for the simultaneous removal of carbon soot and nitrogen oxides from simulated diesel exhaust, J. Phys. Chem. C 118 (2014) 9078–9085.

[6] L. Cheng, Y. Men, J. Wang, H. Wang, W. An, Y. Wang, Z. Duan, J. Liu, Crystal facet-dependent reactivity of α-Mn$_2$O$_3$ microcrystalline catalyst for soot combustion, Appl. Catal. B 204 (2017) 374–384.

[7] N. Feng, J. Meng, Y. Wu, C. Chen, L. Wang, Gao L, H. Wan, G. Guan, KNO_3 supported on three-dimensionally ordered macroporous $La_{0.8}Ce_{0.2}Mn_{1-x}Fe_xO_3$ for soot removal, Catal. Sci. Technol. 6 (2016) 2930–2941.

[8] F. Ji, Y. Men, J. Wang, Y. Sun, Z. Wang, B. Zhao, X. Tao, G. Xu, Promoting diesel soot combustion efficiency by tailoring the shapes and crystal facets of nanoscale Mn_3O_4, Appl. Catal. B 242 (2019) 227–237.

[9] Q. Wu, M. Jing, Y. Wei, Z. Zhao, X. Zhang, J. Xiong, J. Liu, W. Song, J. Li, High-efficient catalysts of core-shell structured Pt@transition metal oxides (TMOs) supported on 3DOM-Al_2O_3 for soot oxidation: the effect of strong Pt-TMO interaction, Appl. Catal. B 244 (2019) 628–640.

[10] Y. Wei, X. Wu, Y. Zhao, L. Wang, Z. Zhao, X. Huang, J. Liu, J. Li, Efficient photocatalysts of TiO_2 nanocrystals-supported PtRu alloy nanoparticles for CO_2 reduction with H_2O: synergistic effect of Pt-Ru, Appl. Catal. B 236 (2018) 445–457.

[11] N. Feng, C. Chen, J. Meng, G. Liu, F. Fang, J. Ding, L. Wang, H. Wan, G. Guan, Constructing a three-dimensionally ordered macroporous $LaCrO_8$ composite oxide via cerium substitution for enhanced soot abatement, Catal. Sci. Technol. 7 (2017) 2204–2212.

[12] M. Machida, Y. Murata, K. Kishikawa, D. Zhang, K. Ikeue, On the reasons for high activity of CeO_2 catalyst for soot oxidation, Chem. Mater. 20 (2008) 4489–4494.

[13] W. Wang, Q. Meng, Y. Xue, X. Weng, P. Sun, Z. Wu, Lanthanide perovskite catalysts for oxidation of chloroaromatics: secondary pollution and modifications, J. Catal. 366 (2018) 213–222.

[14] A. Serve, A. Boreave, B. Cartoixa, K. Pajot, P. Vernoux, Synergy between Ag nanoparticles and yttria-stabilized zirconia for soot oxidation, Appl. Catal. B 242 (2019) 140–149.

[15] L. Castoldi, R. Matarrese, L. Lietti, P. Forzatti, Intrinsic reactivity of alkaline and alkaline-earth metal oxide catalysts for oxidation of soot, Appl. Catal. B 90 (2009) 278–285.

[16] N.E. Olong, K. Stowe, W.F. Maier, A combinatorial approach for the discovery of low temperature soot oxidation catalysts, Appl. Catal. B 74 (2007) 19–25.

[17] M. Piumetti, S. Bensaid, N. Russo, D. Fino, Investigations into nanostructured ceria-zirconia catalysts for soot combustion, Appl. Catal. B 180 (2016) 271–282.

[18] Y. Gao, A. Duan, S. Liu, X. Wu, W. Liu, M. Li, S. Chen, X. Wang, D. Weng, Study of $Ag/Ce_xNd_{1-x}O_2$ nanocubes as soot oxidation catalysts for gasoline particulate filters: balancing catalyst activity and stability by Nd doping, Appl. Catal. B 203 (2017) 116–126.

[19] G.L. Haller, New catalytic concepts from new materials: understanding catalysis from a fundamental perspective, past, present, and future, J. Catal. 216 (2003) 12–22.

[20] A. Setiabudi, M. Makkee, J.A. Moulijn, An optimal NO_x assisted abatement of diesel soot in an advanced catalytic filter design, Appl. Catal. B 42 (2003) 35–45.

[21] H. He, X. Lin, S. Li, Z. Wu, J. Gao, J. Wu, W. Wen, D. Ye, M. Fu, The key surface species and oxygen vacancies in $MnO_x(0.4)$-CeO_2 toward repeated soot oxidation, Appl. Catal. B 223 (2018) 134–142.

[22] C. Cao, X. Li, Y. Zha, J. Zhang, T. Hu, M. Meng, Crossed ferric oxide nanosheets supported cobalt oxide on 3-dimensional macroporous Ni foam substrate used for diesel soot elimination under self-capture contact mode, Nanoscale 8 (2016) 5857–5864.

[23] T. Liu, Q. Li, Y. Xin, Z. Zhang, X. Tang, L. Zheng, P. Gao, Quasi free K cations confined in hollandite-type tunnels for catalytic solid (catalyst)-solid (reactant) oxidation reactions, Appl. Catal. B 232 (2018) 108–116.

[24] T. Kamegawa, N. Suzuki, M. Che, H. Yamashita, Synthesis and unique catalytic performance of single-site Ti-containing hierarchical macroporous silica with mesoporous frameworks, Langmuir 27 (2011) 2873–2879.

[25] Y. Liu, H. Dai, Y. Du, J. Deng, L. Zhang, Z. Zhao, Controlled preparation and high catalytic performance of three-dimensionally ordered macroporous $LaMnO_3$ with nanovoid skeletons for the combustion of toluene, J. Catal. 287 (2012) 149–160.

[26] V. Alcalde-Santiago, A. Davó-Quiñonero, D. Lozano-Castelló, A. Bueno-López, On the soot combustion mechanism using 3DOM ceria catalysts, Appl. Catal. B 234 (2018) 187–197.

[27] T. Kamegawa, N. Suzuki, H. Yamashita, Design of macroporous TiO_2 thin film photocatalysts with enhanced photofunctional properties, Energy Environ. Sci. 4 (2011) 1411–1416.

[28] Y. Wei, J. Liu, Z. Zhao, Y. Chen, C. Xu, A. Duan, G. Jiang, H. He, Highly active catalysts of gold nanoparticles supported on three-dimensionally ordered macroporous $LaFeO_3$ for soot oxidation, Angew. Chem. Int. Ed. 50 (2011) 2326–2329.

[29] Y. Wei, Z. Zhao, X. Yu, B. Jin, J. Liu, C. Xu, A. Duan, G. Jiang, S. Ma, One-pot synthesis of core-shell $Au@CeO_{2-\delta}$ nanoparticles supported on three-dimensionally ordered macroporous ZrO_2 with enhanced catalytic activity and stability for soot combustion, Catal. Sci. Technol. 3 (2013) 2958–2970.

[30] H. Wang, W. Guo, Z. Jiang, R. Yang, Z. Jiang, Y. Pan, W. Shangguan, New insight into the enhanced activity of ordered mesoporous nickel oxide in formaldehyde catalytic oxidation reactions, J. Catal. 361 (2018) 370–383.

[31] M. Mao, H. Lv, Y. Li, Y. Yang, M. Zeng, N. Li, X. Zhao, Metal support interaction in Pt nanoparticles partially confined in the mesopores of microsized mesoporous CeO_2 for highly efficient purification of volatile organic compounds, ACS Catal. 6 (2016) 418–427.

[32] Y. Wei, Z. Zhao, T. Li, J. Liu, A. Duan, G. Jiang, The novel catalysts of truncated polyhedron Pt nanoparticles supported on three-dimensionally ordered macroporous oxides (Mn, Fe, Co, Ni, Cu) with nanoporous walls for soot combustion, Appl. Catal. B 146 (2014) 57–70.

[33] Y. Wei, J. Liu, Z. Zhao, A. Duan, G. Jiang, The catalysts of three-dimensionally ordered macroporous $Ce_{1-x}Zr_xO_2$-supported gold nanoparticles for soot combustion: the metal-support interaction, J. Catal. 287 (2012) 13–29.

[34] Y. Wei, Z. Zhao, J. Liu, S. Liu, C. Xu, A. Duan, G. Jiang, Multifunctional catalysts of three-dimensionally ordered macroporous oxide-supported Au@Pt core-shell nanoparticles with high catalytic activity and stability for soot oxidation, J. Catal. 317

(2014) 62–74.

[35] H. Jiang, T. Akita, T. Ishida, M. Haruta, Q. Xu, Synergistic catalysis of Au@Ag core-shell nanoparticles stabilized on metal-organic framework, J. Am. Chem. Soc. 133 (2011) 1304–1306.

[36] H. Zhang, T. Watanabe, M. Okumura, M. Haruta, N. Toshima, Catalytically highly active top gold atom on palladium nanocluster, Nat. Mater. 11 (2012) 49–52.

[37] J. Plšek, Z. Bastl, Pulsed laser deposition of bimetallic gold-platinum nanoparticles on cerium oxide and their characterisation by X-ray photoelectron spectroscopy and temperature-programmed desorption of isotopically labelled carbon monoxide, J. Catal. 299 (2013) 109–118.

[38] L. Kesavan, R. Tiruvalam, M.H.A. Rahim, M.I. Saiman, D.I. Enache, R.L. Jenkins, N. Dimitratos, J.A. Lopez-Sanchez, S.H. Taylor, D.W. Knight, C.J. Kiely, G.J. Hutchings, Solvent-free oxidation of primary carbon-hydrogen bonds in toluene using Au-Pd alloy nanoparticles, Science 331 (2011) 195–199.

[39] N. Agarwal, S.J. Freakley, R.U. McVicker, S.M. Althahban, N. Dimitratos, Q. He, D.J. Morgan, R.L. Jenkins, D.J. Willock, S.H. Taylor, C.J. Kiely, Graham J. Hutchings, Aqueous Au-Pd colloids catalyze selective CH_4 oxidation to CH_3OH with O_2 under mild conditions, Science 358 (2017) 223–227.

[40] S. Xie, J. Deng, S. Zang, H. Yang, G. Guo, H. Arandiyan, H. Dai, Au-Pd/3DOM Co_3O_4: highly active and stable nanocatalysts for toluene oxidation, J. Catal. 322 (2015) 38–48.

[41] M. Cargnello, J.J.D. Jaén, J.C.H. Garrido, K. Bakhmutsky, T. Montini, J.J.C. Gámez, R.J. Gorte, P. Fornasiero, Exceptional activity for methane combustion over modular $Pd@CeO_2$ subunits on functionalized Al_2O_3, Science 337 (2012) 713–717.

[42] X. Weng, Q. Meng, J. Liu, W. Jiang, S. Pattisson, Z. Wu, Catalytic oxidation of chlorinated organics over Lanthanide perovskites: effects of phosphoric acid etching and water vapor on chlorine desorption behavior, Environ. Sci. Technol. 53 (2019) 884–893.

[43] N. Serhan, A. Tsolakis, A. Wahbi, F.J. Martos, S. Golunski, Modifying catalytically the soot morphology and nanostructure in diesel exhaust: influence of silver De-NO_x catalyst (Ag/Al_2O_3), Appl. Catal. B 241 (2019) 471–482.

[44] J. Xiong, Q. Wu, X. Mei, J. Liu, Y. Wei, Z. Zhao, D. Wu, J. Li, Fabrication of Spinel-type $Pd_xCo_{3-x}O_4$ binary active sites on 3D ordered meso-macroporous Ce-Zr-O_2 with enhanced activity for catalytic soot oxidation, ACS Catal. 8 (2018) 7915–7930.

[45] Y. Wei, J. Jiao, X. Zhang, B. Jin, Z. Zhao, J. Xiong, Y. Li, J. Liu, J. Li, Catalysts of self-assembled $Pt@CeO_{2-\delta}$-rich core-shell nanoparticles on 3D ordered macroporous $Ce_{1-x}Zr_xO_2$ for soot oxidation: nanostructure-dependent catalytic activity, Nanoscale 9 (2017) 4558–4571.

[46] Y. Wei, J. Liu, Z. Zhao, A. Duan, G. Jiang, C. Xu, J. Gao, H. He, X. Wang, Three-dimensionally ordered macroporous $Ce_{0.8}Zr_{0.2}O_2$-supported gold nanoparticles: synthesis with controllable size and super-catalytic performance for soot oxidation, Energy Environ. Sci. 4 (2011) 2959–2970.

[47] H. An, Z. Chen, J. Yang, Z. Feng, X. Wang, F. Fan, C. Li, An operando-Raman study on oxygen evolution of manganese oxides: roles of phase composition and amorphization, J. Catal. 367 (2018) 53–61.

[48] M. Yashima, H. Arashi, M. Kakihana, M. Yoshimura, Raman scattering study of cubic-tetragonal phase transition in $Zr_{1-x}Ce_xO_2$ solid solution, J. Am. Ceram. Soc. 77 (1994) 1067–1071.

[49] W. Weber, K. Hass, J. McBrige, Raman study of CeO_2: second-order scattering, lattice dynamics, and particle-size effects, Phys. Rev. B 48 (1993) 178–185.

[50] R. Si, Y. Zhang, S. Li, B. Lin, C. Yan, Urea-based hydrothermally derived homogeneous nanostructured $Ce_{1-x}Zr_xO_2$ (x = 0–0.8) solid solutions: a strong correlation between oxygen storage capacity and lattice strain, J. Phys. Chem. B 108 (2004) 12481–12488.

[51] W. Tang, Z. Hu, M. Wang, G.D. Stucky, H. Metiu, E.W. Mcfarland, Methane complete and partial oxidation catalyzed by Pt-doped CeO_2, J. Catal. 273 (2010) 125–137.

[52] Z. Wu, X. Lin, H. He, M. Fu, D. Ye, Evolution of key surface species on MnO_x-CeO_2 in pulse dielectric barrier discharge towards soot oxidation, Acta Sci. Circum. 37 (2017) 863–870.

[53] Y. Ji, D. Xu, S. Bai, U. Graham, M. Crocker, B. Chen, C. Shi, D. Harris, D. Scapens, J. Darab, Pt- and Pd-promoted CeO_2-ZrO_2 for passive NO_x adsorber applications, Ind. Eng. Chem. Res. 56 (2017) 111–125.

[54] Y. Liu, B. Liu, Y. Liu, Q. Wang, W. Hu, P. Jing, L. Liu, S. Yu, J. Zhang, Improvement of catalytic performance of preferential oxidation of CO in H_2-rich gases on three-dimensionally ordered macro- and meso-porous Pt-Au/CeO_2 catalysts, Appl. Catal. B 142-143 (2013) 615–625.

[55] L.F. Liotta, A. Longo, A. Macaluso, A. Martorana, G. Pantaleo, A.M. Venezia, G. Deganello, Influence of the SMSI effect on the catalytic activity of a Pt(1%)/$Ce_{0.6}Zr_{0.4}O_2$ catalyst: SAXS, XRD, XPS and TPR investigations, Appl. Catal. B 48 (2004) 133–149.

[56] M. Bosco, M. Banares, M. Huerta, A. Bonivardi, S. Collins, In situ FTIR and Raman study on the distribution and reactivity of surface vanadia species in V_2O_5/CeO_2 catalysts, J. Mol. Catal. A 408 (2015) 75–84.

[57] C. Davies, K. Thompson, A. Cooper, S. Golunski, S.H. Taylor, M.B. Macias, O. Doustdar, A. Tsolakis, Simultaneous removal of NO_x and soot particulate from diesel exhaust by in-situ catalytic generation and utilisation of N_2O, Appl. Catal. B 239 (2018) 10–15.

[58] W. Lin, A.A. Herzing, C.J. Kiely, I.E. Wachs, Probing metal-support interactions under oxidizing and reducing conditions: in situ Raman and infrared spectroscopic and scanning transmission electron microscopic-X-ray energy-dispersive spectroscopic investigation of supported platinum catalysts, J. Phys. Chem. C 112 (2008) 5942–5951.

[59] S. Liu, X. Wu, W. Liu, W. Chen, R. Ran, M. Li, D. Weng, Soot oxidation over CeO_2 and Ag/CeO_2: factors determining the catalyst activity and stability during reaction, J. Catal. 337 (2016) 188–198.